MICROSENSORS FOR CHEMICAL AND ONCOLOGICAL APPLICATIONS

A Dissertation

Presented to the Faculty of the Graduate School

of Cornell University

In Partial Fulfillment of the Requirements for the Degree of

Doctor of Philosophy

by

Daniel Juhyung Joe

August 2014

MICROSENSORS FOR CHEMICAL AND ONCOLOGICAL APPLICATIONS

Daniel Juhyung Joe, Ph. D.

Cornell University 2014

This dissertation presents characteristics and utilities of enhanced microsensors for chemical land oncological applications. Simple and cheap techniques for fabrication of mechanical and electrical sensing devices in micro scale have been developed. Critically buckled resonant microbrides with active sensing polymer layer detect chemical gases as it swells volumetrically and its resonant frequency shifts due to altered tension in the microbridges. Substantial improvements in quality factor and frequency stability of the microresonators under ambient pressure and temperature condition have been demonstrated. For potential applications in monitoring electrical behavior of human colorectal carcinoma cells, bio-functionalized electrical graphene microsensors on a sapphire substrate have been developed. The biosensors have shown substantial increase in impedance compared to its baseline with a small number of captured cells. In addition to the development of microsensors, experimental procedure for visualization of metastatic colorectal tumor cells in mice using multi-photon fluorescent microscopy is presented.

BIOGRAPHICAL SKETCH

Daniel Juhyung Joe was born in 1985, in Haenam, a small town located in the southwest of South Jeolla Province, Republic of Korea (or South Korea). His parents are Jum-Shim Kim (in Korean culture women do not change their last names after marriage) and I-man Joe, who have sacrificed anything for my expensive and time-consuming education. When he was nine years old, Daniel and his family have moved to a port city called Mokpo, South Jeolla Province. His younger brother and parents still live in the same city. When he was fifteen years old, Daniel decided to come to the United States for his future education. While his uncle has been a guardian, he attended high school in Champaign, IL, graduating in 2004. He received B.S. degree in Electrical Engineering with minor in physics at the University of Illinois at Urbana-Champaign in 2008. During his college years, Daniel has been highly interested in micro- and nanofabrication technology for semiconductor devices. He, however, realized that the funding situation would become more promising if working in the area of biological and chemical microsensors rather than traditional semiconductor devices. During six years of training in the ECE graduate program at Cornell University, Daniel has gained various experience regarding microsensor technologies in diverse applications. After his graduation, Daniel will search for a governmental research job position in his country, which can effectively replace his military responsibility as a Korean citizen. Besides scientific research activities, he has also had other interests, especially in translation services and electronic sports (or esports). In addition to his research career, Daniel hopes to extend his interests in esports and translation services to a professional level if time permits and opportunity is given.

Dedicated to my parents

ACKNOWLEDGMENTS

The work presented in this dissertation has been supported by various funding sources that include the Cornell Nanobiotechnology Center (NBTC), Cornell Nanoscale Facility (CNF), the Cornell Center for Materials Research (CCMR), the National Science Foundation (NSF) and the National Institutes of Health (NIH). It would be impossible for me to carry out this work without help from a number of people during my graduate program at Cornell. Collaborators who deserve credits for significant amount of help and support for my research include Yoav Linzon, Slava Krylov, Moonkyung Kim, Jeonghyun Hwang, Ben Cipriany, Tiberiu Onuta, Paula Miller, Jiahn Choi, Poornima Gadamsetty, James Shealy, Nikolai Rakhilin, Huanhuan Joyce Chen, and Christelle Johnson. Other individuals who deserve thanks for helpful advice and discussions include Seung-min Park, Darren Southworth, Vivek Adiga, Rob Barton, Rob Ilic, Aline Cerf, Kylan Szeto, Yong-Jun Shin, Mandy Esch, Phengcheng Bu and Lihua Wang. Cornell faculty members who have helped me by providing opportunities for productive collaborations include Jeevak Parpia, Michael Shuler, Steven Lipkin, Brian Kirby, Nozomi Nishimura, Chris Schaffer and Michael Spencer. And finally, I truly thank Harold Craighead and Xiling Shen who have patiently guided me, served on various forms as an advisor, and provided me scientific motivation and inspiration through the years.

TABLE OF CONTENTS

CHAPTER 1

INTRODUCTION

1.1 Introduction and Overview

Microelectromechanical systems (MEMS), the technology of miniaturized devices, incorporate a range of useful functionalities, both electrical and mechanical, into a small chip-scale package. With dimensions on the order of microns (10^{-6} m) or less, these systems range from complex machines to simple flexural elements, and typically include some form of electrical or optical integration. Devices are often fabricated using microelectronics technology. Successfully fabricated and marketed MEMS technologies include airbag accelerometers, injet printer nozzles, micromirrors for projector and television displays, and motion sensors (such as accelerometers and gyroscopes) for video game controllers. Further promising applications of microdevices include sensors of pressure[1,2], temperature[3-5], charge[6], spin[7] and mass[8-15]. This kind of sensing applications is benefited by moving to smaller size scales. Smaller devices have the potential to consume less power and offer greater sensitivity than their larger scale mechanical or electrical counterparts.

In this dissertation, issues related to the characteristics and utility of improved microsensors will be discussed. Specific achievements presented in this work will include the development of simple and cheap techniques for fabricating mechanical and electrical sensing devices in micro scale, demonstration of sensing chemical vapors in ambient conditions using critically buckled doubly clamped functionalized mechanical resonators, and the use of graphene nanosheets for a novel electrical

biosensor to detect large-sized bio-species such as cancer cells. In addition to the development of microsensors, visualization of invading colorectal cancer cells with multi-photon microscopy using genetically engineered mouse models (GEMM) will be discussed.

1.2 Stress-based Resonant Micro Gas Sensors

1.2.1 Comparison with Other Micro Gas Sensors

There is great demand for fast, sensitive, and inexpensive gas sensors. Aiming towards large-scale lab-on-a-chip integration, the development of microsensors implemented by micro and nanoelectromechanical systems (M/NEMS)[16,17] are being adopted for biological, chemical, and environmental sensing applications[18–21]. For example, in biomedical and clinical studies, miniaturized olfactory microsensors can diagnose diseases such as asthma and diabetes through exhaled breath analysis[22–24]. Miniaturized chemical gas sensors have been developed to detect very small amounts of flammable gases and trace explosive gases for public safety and security uses[25–28]. In these applications, different types of chemical microsensors have been investigated, including deflection-based functionalized MEMS cantilever arrays[29,30], chemiresistors[31], capacitive chemical microsensors[32], nanowire arrays[28,33], quartz crystal microbalance (QCM)[34], surface acoustic wave (SAW) devices[35,36], and mass-based detection in NEMS arrays[37,38]. Table 1.1 summarizes estimated sensitivities and response times of some of these methods.

Methods	Estimated Response Time	Estimated Minimum Detectable Concentration	Pressure and temperature	Analyte
Deflection-based MEMS array[29]	~ 50 s	1000 ~ 2000 ppm	atmosphere, room temperature	water, ethanol, acetone, etc.
Chemiresistor[31]	~10 ms	4~5 ppm	atmosphere, room temperature	methanol, water, benzene, etc.
Nanowire array[33]	~ 10 s	0.1~1 ppm	atmosphere, 300 °C	ethanol
Mass-based detection in MEMS array[37]	40 ms	0.6 ppb	atmosphere, 40 °C	toluene, octane, etc.

Table 1.1 Estimated response time and minimum detectable concentration among selected methods for micro- and nano- gas sensors

1.2.2 Previous Work and Motivation

In previous work, the stress-based detection approach and water vapor detection in silicon-polymer composite resonant microbridges (RMBs)[39] has been demonstrated. Doubly clamped RMBs functionalized with thermally evaporated nanoporous polymer film exhibited significant positive resonant frequency shifts in a silicon-polymer bilayer due to stress changes from adsorbed vapors that cause the polymer layer to swell. This mechanism is dominant over mass-loading effects from the vapors that would induce negative frequency shifts. The RMBs under compressive stress have a calculated sensitivity as low as 170 parts-per-million (ppm) with a response time of few seconds[39].

In this dissertation we present the resonant response of polymer-spincoated doubly-clamped beams to ethanol, benzene and water vapor. Our beams operate near their critical bucking stress[40] (also known as the Euler stress), where the sensitivity of the devices is potentially greater than cantilevers or doubly-clamped beams far away from the critical stress. This critical stress, σ_{crit}, is known to be

$$\sigma_{crit} = \frac{\pi^2}{3}\frac{Et^2}{l^2} \tag{1.1}$$

where E is the Young's modulus, t is the thickness, and l is the effective beam length. Here we demonstrate functionalization of reproducible spin coated polymer layer of a few tens of nanometers thickness on top of 140 nm thick near-critically buckled microbridge resonators, yielding sensitivity and response time comparable to state-of-art devices[29-38].

1.3 Electrical Graphene Biosensors

Graphene, a two-dimensional single or a few sheets of sp^2-hybridized carbon atoms, exhibits exceptional material properties such as high intrinsic carrier mobility, semi-metallic properties, high optical transparency and high surface area-to-mass ratio at room temperature[41-45]. In addition to its unique properties, graphene is a potential alternative to carbon nanotube (CNT) structures for certain applications. For instance, it is known to be difficult to manipulate CNTs for device fabrication if only a few CNTs are used[46,47]. Two-dimensional planar structure of graphene allows for simpler

device process and more complex integration using established semiconductor processes. Additionally, its high Young's modulus and optical transparency is remarkably useful to fabricate competent optical devices and sensors implemented by nanoelectromechanical systems (NEMS)[44,48.49]. As it exhibits unique and attractive properties, graphene has been considered to be a novel nanomaterial for biological and chemical sensor development in various applications[50,51]. These include detection of gases[52], pH[53], cells[54-56], bacteria[57], and biomolecules such as glucose, DNA, and protein[58-62]. Graphene-based biosensors, for example, have shown advantages such as improved detection sensitivity due to high surface area-to-volume ratio, unique optical properties, and ease of effective surface modification[63,64].

In this work, we describe simple, label-free electrical impedance detection of cancer cells using bio-functionalized graphene on sapphire substrate. A single or a few nanosheets of high-quality graphene film is grown using a catalyst-free chemical vapor deposition (CVD) method, confirmed by both Raman spectroscopy and atomic force microscopy (AFM)[65,66]. Fabricated using traditional microfabrication technology, the electrical graphene biosensors are structurally simple with size-controlled graphene sensing surface and easily operated without presence of solution-gate. The graphene active surface is coated with immoblizied the Epithelial Cell Adhesion Moledule (EpCAM) antibodies, which capture human colorectal carcinoma cells and result in changes in conductance. With a low electric field that avoids any damage to biomolecules or cells, a small number of captured cells cause impedance changes as large as ~20% of the baseline value in the functionalized graphene microsensors.

1.4 3D Printed Intestinal Stage for Visualization of Metastatic Colorectal Cancer

Colorectal cancer (CRC) is a leading cause of cancer death worldwide[67,68]. As they proliferate through multiple distinct stages, CRCs eventually acquire the ability to invade outside the colorectum and metastasize into difference organs such as liver lung, and peritoneum[69,70]. When metastatic CRCs are treated with chemotherapy, they almost invariably become chemoresistant. Consequently, five-year survival for patients with metastatic CRCs is only ~15% and, despite recent advances, current chemotherapy regimens almost never cure advanced disease.

Two-photon fluorescence microscopy is used to image CRC metastasis in live mouse tissue. This direct visualization approach has the ability to track fluorescently labeled metastatic CRCs at single cell level. Under isoflurane anesthesia, a portion of the small intestine (for non-survival surgery) is externalized in order to visualize metastatic CRCs from the orthotopic tumor. The mouse intestine is covered with a glass coverslip and supported by a 3D printed intestinal stage for improved stability and imaged with a custom-built multiphoton microscope optimized for *in vivo* imaging. Vasculature is labeled with an intravenous injection of dextran labeled dye, which allows better visualization of labeled intravasating tumor cells. This approach has the potential to capture fluorescently labeled human CRC cells in the process of intravasating and disseminating through the vasculature in live animal models, which provides profound insights into the mechanism of metastasis.

CHAPTER 2

BUCKLED BEAM MECHANICAL RESONATOR

2.1 Introduction

In this chapter we describe sensing of chemical vapors from the atmosphere using critically buckled polycrystalline silicon doubly-clamped mechanical resonators. Our method of sensing is based on stress-induced resonant frequency shifts through volumetric swelling of the 60 nm thick polymethyl methacrylate layer resulting in altered tension in the beams. The stress change produces shifts in the resonant frequency as large as 150 % of the baseline frequency. In order to maximize the sensitivity, we tailor residual stress of the polycrystalline silicon resonators to slightly exceed the critical buckling stress. We incorporate a relatively large gap between the bridge and a substrate to provide optical readout and minimize squeezed film effects. We show that the larger gap results in substantial improvements of the quality factor and frequency stability of our resonators under ambient pressure and temperature conditions compared to previous implementations. These lead to resonant frequency shift per concentration change of ethanol vapors of ~360 Hz/ppm with a response time of a few seconds measured in our gas delivery and readout system.

2.2 Fabrication and Operation of Resonant Microbridges for Gas Sensing

Established lithographic fabrication techniques have been developed for the micro gas sensor reported in this dissertation. Most of the fabrication work was performed in the Cornell Nanoscale Science and Technology Facility (CNF).

Substrates consisted of thin films grown on single crystal silicon handle wafers, which are typically ~500 μm thick and 4 inch diameter. The resonant microbridges (RMBs) are fabricated using n+ doped polycrystalline silicon (poly-Si) films grown by low pressure chemical vapor deposition (LPCVD) at 596 ± 3 °C on top of a thermal sacrificial oxide layer. The deposition temperature controls the residual stress in the poly-Si layer and is selected to consistently yield near-critically buckled 20 μm long and 140 nm thick resonators. The thickness of the poly-Si film is approximately 140 nm, while that of the sacrificial oxide is 1.2 μm, both of which are deposited on a (100) silicon substrate. Doubly clamped beams that are 20 μm long and 2 μm wide are patterned, followed by HF wet-etch release and critical point drying (CPD) of the suspended beams. The CPD is used to prevent stiction in the device. The residual compressive film stress is relieved upon the wet-etch release of the beams, which cause the RMBs to be slightly buckled either out of plane or towards the silicon backplane. Prior to their surface functionalization, we deposit a 1H, 1H, 2H, 2H-perfluorooctyltrichlorosilane (FOTS) monolayer coating on top of the doubly clamped RMB and substrate surface by molecular vapor deposition (MVD). This FOTS monolayer film, which makes the resonator surface substantially hydrophobic, prevents stiction of the bridges to the substrate during the last spin coating process of the functionalizing polymer. A brief low-power oxygen plasma etch removes the FOTS coating from the top surface of the wafer. Approximately 60 nm of polymethyl methacrylate (PMMA) is then deposited by spin coating method, a polymer known as effective for sensing flammable vapors[71]. The thickness of our PMMA layer is estimated by spin coating a separate silicon piece under the same spin conditions

(measured by FilMetrics F40 (San Diego, CA, USA)). A schematic of our fabrication process is illustrated in Figure 2.1. Both optical microscope and scanning electron microscope (SEM) images of the spin coated RMBs, which are presented in Figure 2.2, show that the bridges are buckled and that the spin coated PMMA adhered to the top of the bridges. We find that the midpoint displacements of the non-coated and PMMA-coated RMBs are 137 and 265 nm toward the substrate (~1% of the beam length) as measured by an optical surface profiler (Zygo, Middlefield, CT, USA). Therefore, the RMBs are near their critically buckled state. In case that the deposition temperature of poly-Si films during the LPCVD process is considerably higher than the selected temperature (~596 ºC), we find that the amount of compressive stress exerted in its axial direction notably exceeds the Euler stress given by eq. (1.1), which causes the RMB to be highly buckled[72]. An example of a highly buckled RMB prior to the functionalization is shown in Figure 2.3.

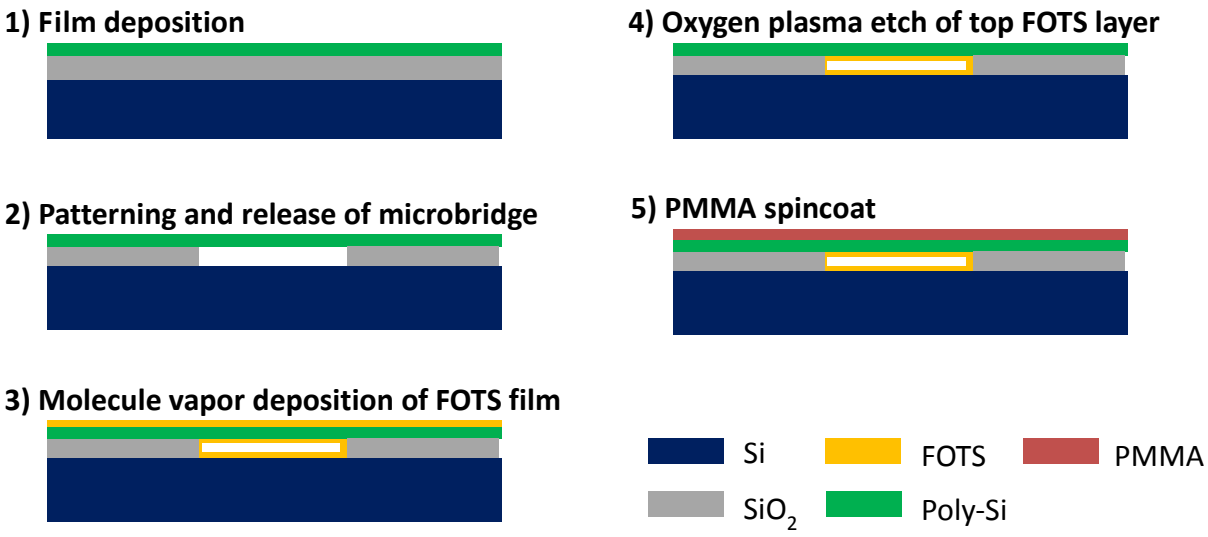

Figure 2.1 Fabrication process of a critically buckled micromechanical resonator functionalized with PMMA spin coating. Buckling of the bridges is not depicted in this figure.

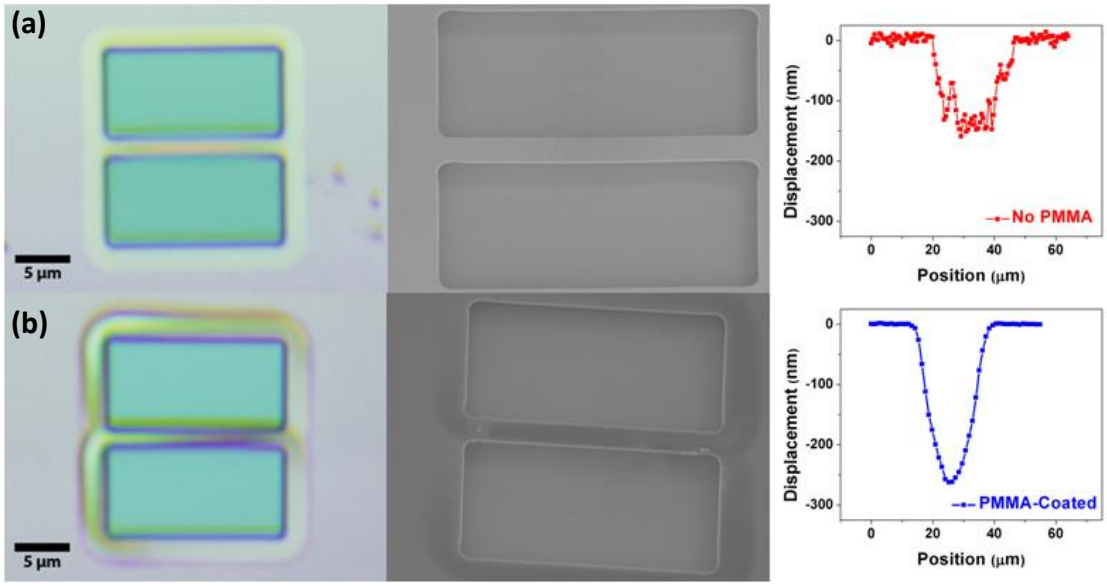

Figure 2.2 Optical microscope (left), SEM image tilted by 30 degrees (middle), and surface profile (right) of the micromechanical bridge (a) before (top) and (b) after (bottom) its functionalization, respectively (20 µm × 2 µm × 0.14 µm).

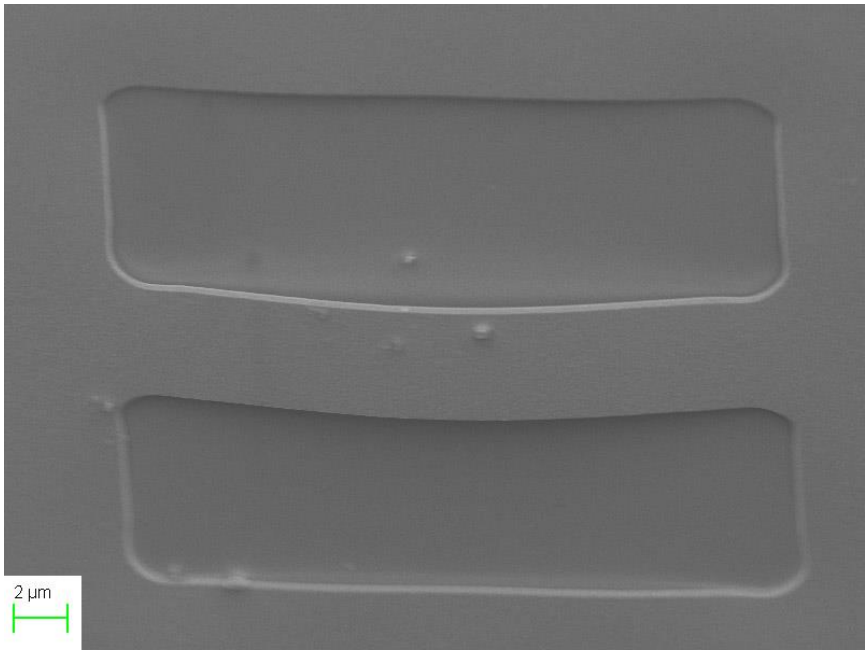

Figure 2.3. SEM image of a highly buckled RMB with dimensions and residual stress values significantly different than in Figure 2.2 (dimensions: 25 µm × 6 µm × 0.14 µm)

Before their functionalization, the RMBs are wire bonded and mounted on a dual-in-line package (DIP), after which they are loaded into a flow chamber for device characterization (See Figure 2.4). The experimental setup for gas delivery and resonant measurements is described in Figure 2.5, whereas gas concentrations are mixed through a dual channel flow-line[39]. The doubly clamped beams are driven by electrostatic force between the RMBs and the substrate through a spectrum analyzer, which is coupled with DC biasing voltage, and their out of plane motion is detected using an interferometric optical technique[73]. In order to maximize the optical reflectance signal, the gap between the poly-Si bridge and the substrate is chosen to be 1.2 μm. The resonance spectrum of the bridges is monitored, as mixtures of dry nitrogen and vapor of interest with various concentrations, are delivered to the devices through the flow line system. Concentrations are controlled by mass flow controllers in each of two flow channels. The desired concentration of analyte vapor is obtained by altering the ratios of dry nitrogen and analyte vapor through the liquid state analytes. Here we assume that vapors from the analyte channels are fully saturated. Under this assumption and through knowledge of the mixing ratio, we obtain the analyte concentration in parts-per-thousand (ppt) in the high concentration range and parts-per-million (ppm) in the low concentration range. Before each set of measurements, saturated ethanol vapor is loaded into the flow chamber and then fully vented after a few minutes in order to effectively purge the flow chamber, resetting the RMB near the critically-buckled and dry state.

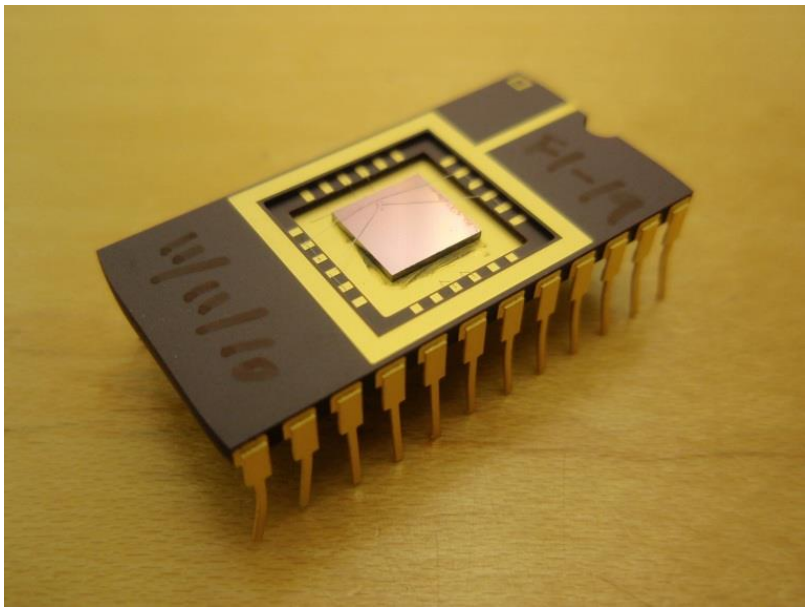

Figure 2.4 Wire-bonded device chip mounted on a dual in-line package

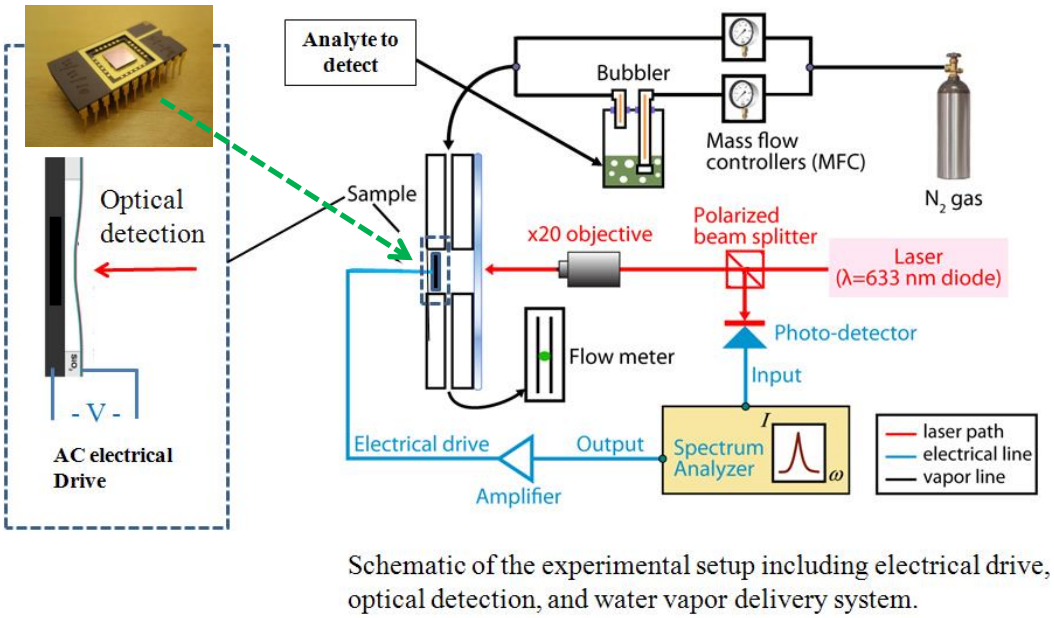

Figure 2.5 Comprehensive schematic of the experimental setup for stress-based resonant microbridge

2.3 Resonance Characteristics

According to the derivation in Appendix A, the fundamental frequency of microbridges in the first buckled configuration f_0 can be approximated by

$$f_0 = 2\pi\sqrt{\frac{2EI}{3mL^4}\left(\frac{\sigma}{\sigma_E}-1\right)} \tag{2.1}$$

where σ is the axial compressive stress and $\sigma_E = 4\pi^2 Er^2/L^2$ is the Euler's buckling stress. Resonant frequency shift Δf_0 resulting from small effective mass and axial stress variations only (Δm and $\Delta\sigma$, respectively) without other stiffness property variations, can be approximated to the first order by the expansion

$$\frac{\Delta f_0}{f_0} = \frac{1}{2}\left(-\frac{\Delta m}{m}+\frac{\Delta\sigma}{\sigma-\sigma_E}\right) \tag{2.2}$$

According to eq. (2.2), the resonant frequency may drop due to loaded analyte mass ($\Delta m>0$) or increase due to altered axial stress exerted to the functionalized resonant microbridge (RMB) ($\Delta\sigma$). For a buckled RMB, swelling of the polymer layer alters the stress of the bridges towards more compressive as it reacts with the analyte, causing a positive $\Delta\sigma$ and a rise in the resonant frequency. On the other hand, the frequency decreases in a pre-buckled RMB configuration when compressive stress is applied as it induces negative change in $\Delta\sigma$. As the RMB approaches closer to its critical buckling state, the difference between the axial and Euler stress becomes much smaller, which results in relatively higher induced change in normalized axial stress,

or $\Delta\sigma/(\sigma-\sigma_E)$. (Note that an additional increase in the sensitivity can be expected due to the influence of the stress gradient between the polymer layer and the beam) In case of a flat beam structure, however, change in the normalized axial stress is much smaller than that of a critically buckled RMB, and other stiffness changes might become more dominant. Providing large increase in its resonant frequency due to introduction of each analyte, the functionalized RMB has fundamental mode resonant frequencies of 1.3, 2.7, 2.9 and 3.6 MHz in dry nitrogen, saturated water, benzene, and ethanol vapor, respectively (See Figure 2.6). These values are obtained without significant deterioration of the functionalized surface, allowing numerous cycles of consistent device operation with the analytes chosen for this study.

Figure 2.7 shows time traces of the functionalized micromechanical resonator response for each saturated analyte vapor. For saturated ethanol vapor, approximately 2 MHz increase in the resonant frequency (that is, ~150 % of the baseline frequency with dry nitrogen) has been observed, while less than 0.5% increase in its normalized resonant frequency has been observed for the non-spincoated RMB that has only the FOTS layer. In addition to rise in resonant frequency unique to each saturated analyte, the frequency-time trace may be indicative for each chemical. The time response for each analyte absorbed into the polymer coating can be modeled as a solution of the Fick's law of diffusion in terms of a series of exponential terms[74,75]. To first order approximation, assuming that the resonant frequency shifts are linearly proportional to the ratio of vapors diffused into the polymer at a given time, we model the resonant frequency as an exponential relaxation function[76] to extract the response time constant, which we define as the time taken to achieve 70% of the total frequency shift. Time

constants of 8.4, 11.7, and 26.9 seconds have been measured for the spin coated RMB with the injection of saturated ethanol, water and benzene vapor into the flow chamber, respectively (See Figure 2.7). For the ethanol vapor, we observe that the resonant frequency overshoots, but this effect is not seen for diluted ethanol vapor whose concentration is 2.9 ppt (See Figure 2.7) or less.

The relationship between resonant frequency and squeeze film effect in the RMBs is examined. The squeeze film effect governs the gas flow between a microbridge and substrate moving towards each other. If the bridge moves slowly, gas is squeezed out and dissipation loses result. For fast movement, it compresses the air, resulting in spring forces. According to Blech[77], a characteristic dimensionless squeeze number, σ_{sqn}, can be defined as

$$\sigma_{sqn} = \frac{12\mu a^2 \omega}{P_a d^2} \tag{2.3}$$

where d is the distance between the substrate and the resonator, P_a is the ambient pressure, μ is the viscosity of air, and a is the typical dimension (or the width for a doubly clamped beam structure) of the RMB. For a low squeeze numbers (and frequencies), the air can flow out from below the resonator without compression and thus there is no significant fluid increase in the device stiffness. On the other hand, at high squeeze numbers, the gas does not have sufficient time to flow out from below the device and the air acts like a compressible spring. The squeeze number for our

RMB is estimated to be σ_{sqn} = 0.074 << 10, so that the ambient pressure gas is not trapped under the resonator but readily flows from the compressed area.

The significantly reduced squeeze film damping effect is due to a relatively large gap (~1.2 μm) between the resonator and the substrate that leads to a higher qualify factor[74]. In Figure 2.6, the functionalized RMB has fundamental mode quality factors of 8.7, 23.7, 26.6 and 28.8 in dry nitrogen, saturated water, benzene, and ethanol vapor, respectively. This provides an improvement of more than a factor of two in the quality factor in comparison with previous implementations[39] in ambient condition because of reduction in energy dissipation of the RMB due to the reduced squeeze film damping. Figure 2.8 shows that despite the decrease in amplitude, as the resonant frequency shifts upward, the quality factors of the resonators scale with resonant frequency as vapors are introduced into the flow chamber, similar to the mechanical behavior in other mechanical resonators in air[78,79]. This also suggests that the mechanical behavior of the bilayer is strongly dominated by the poly-Si RMB, where as the PMMA layer serves mostly to introduce stress changes only. The magnitudes of resonant frequency shifts (dry nitrogen, water, benzene, and ethanol by increasing order) and frequency dependence of quality factor have been reproducibly observed in several devices functionalized by the same protocol in our laboratory.

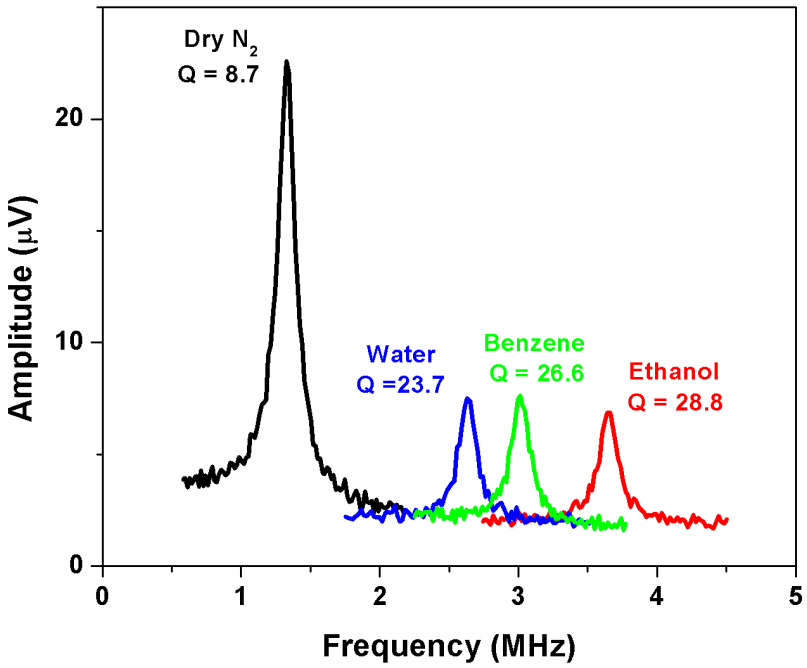

Figure 2.6 The resonant peaks and qualify factors of a resonant micromechanical bridge surrounded by saturated analyte vapor before baseline subtraction

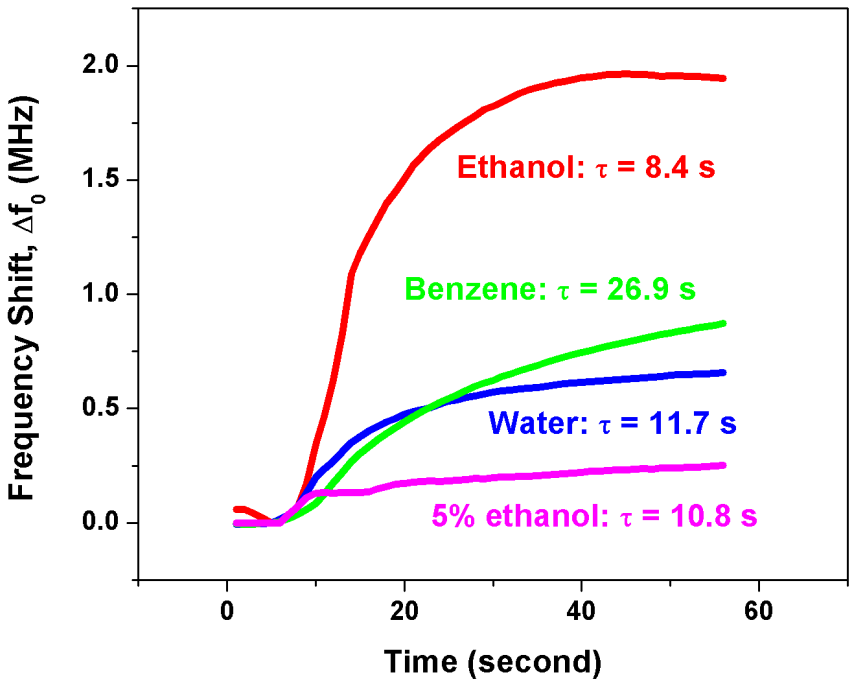

Figure 2.7 Resonant frequency shift evolution in time of the functionalized micromechanical resonator after exposure to individual saturated analytes following baseline subtraction. In order to extract the response time constant τ, we define as the time taken to achieve 70% of the total frequency shift. In case of ethanol vapor, whose concentration is greater than 2.9 parts-per-thousand, resonant frequency overshoot effect has been observed.

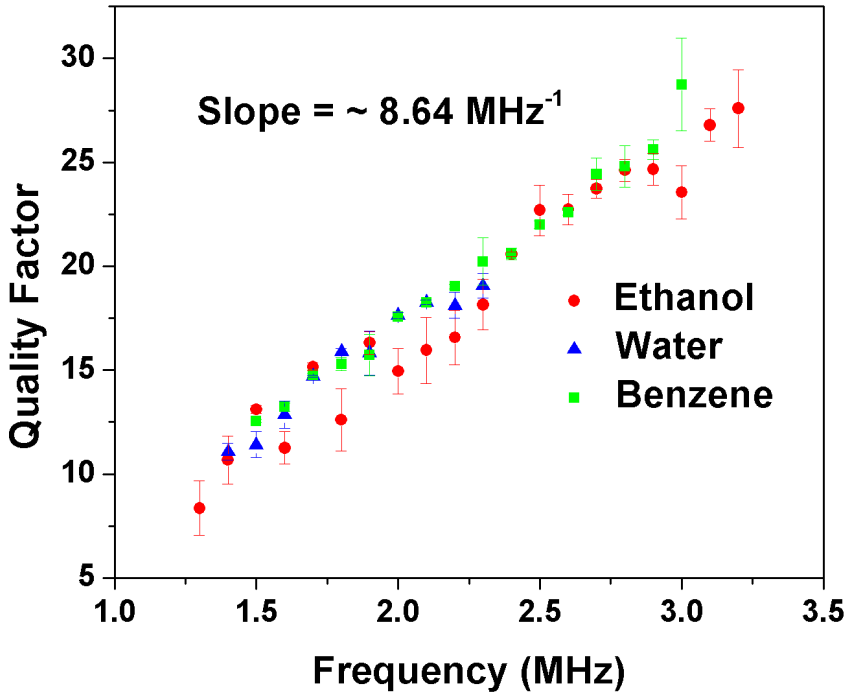

Figure 2.8 Quality factor vs. resonant frequency of the RMB ($\Delta Q/\Delta f$ = 8.64 MHz^{-1})

2.4 Device Performance

In order to characterize vapor detection sensitivity of functionalized RMBs, we first consider basic limits on our device performance. One important consideration is the pressure dependence of the RMB's resonant frequency. According to eq. (2.3), the squeeze number is very low, which ensures that the RMB is not in the regime where the resonant frequency increases linearly with the pressure[80-82]. Instead, the resonant frequency actually decreases in our experiment as the pressure inside the flow cell increases presumably due to mass entrainment[83]. For example, Figure 2.9(a) shows an example of the averaged resonant frequency variations of the RMB due to pressure variations inside the flow chamber. Here, the sign of the frequency change is opposite to that introduced by swelling of the polymer layer. Frequency shift per unit pressure change ($\Delta f/\Delta P$) is measured to be -3.86 ± 0.41 kHz/Torr, while the temperature is kept stable throughout the experiments. The flow rate of dry nitrogen is fixed as 10,000 sccm for this measurement, which causes an increase in pressure of about 16 Torr inside the flow chamber. However, pressure fluctuation for a nominally constant dry nitrogen flow is found to be 0.32 ± 0.05 Torr as measured for an hour. In addition to the frequency change observed due to the pure pressure variation, we note that due to the imbalance in our flow system there is a small pressure rise per ethanol concentration increase $(\Delta P/\Delta C)$. This is measured to be 0.36 ± 0.08 Torr/ppt (See Figure 2.9(b)). Combining these results by multiplying $\Delta f/\Delta P$ with $\Delta P/\Delta C$, the frequency shift per change in ethanol concentration contributed by pressure change, $\Delta f/\Delta C_{,pressure}$, is estimated to be only -1.39 Hz/ppm. It is essential for the RMB to

achieve vapor detection sensitivity higher than this value, in order to accurately sense the analyte vapor.

Other important considerations regarding limits on our device performance are baseline frequency drift and noise. The resonant frequency of the RMB surrounded by flowing dry nitrogen gas represents the baseline measurement. The baseline exhibits a slow, but continuous exponential drift with a characteristic time constant that is two orders of magnitude greater than the response time to typical analyte vapors. After the ethanol purge is completed, the overall magnitude of rise in the baseline during the course of the measurement is ~ 120 kHz in average for each run (usually 30 minutes – 1 hour). An example of the natural baseline drift is shown in Figure 2.10(a). We speculate this slowly upward-drifting baseline frequency as effects of either moisture from the environment, or a slow stress-strain relaxation of the buckled beam. Similar results in the resonant frequency shifts have been obtained for each run in spite of the baseline rises. For further analysis, the exponential-like baseline is subtracted from the observed resonant frequency. For example, Figure 2.10(a) shows steps of frequency rises upon increase in vapor concentration before and after baseline subtraction.

In addition to the long-term frequency drifts, short-term frequency noise also limits vapor detection resolution of the functionalized RMBs. For instance, Figure 2.10(b) illustrates an example of such frequency noise. In this figure, the short term frequency noise, Δf_{noise}, which represents a standard deviation of the frequency fluctuations in a minute, is measured to be approximately $\Delta f_{noise} = \pm$ 0.25 kHz. Compared to the width of the resonant frequency, Δf_0 (= ~200 kHz), this frequency noise component is very small (that is, ~0.25 % of Δf_0). We believe that this frequency

noise is mainly due to thermal fluctuations in the polymer coating around the detection laser spot, which adds to other sources of frequency noise. Pressure fluctuations combined with the baseline rise and frequency noise sets the resolution limit of our vapor sensing method with the current gas delivery and readout system.

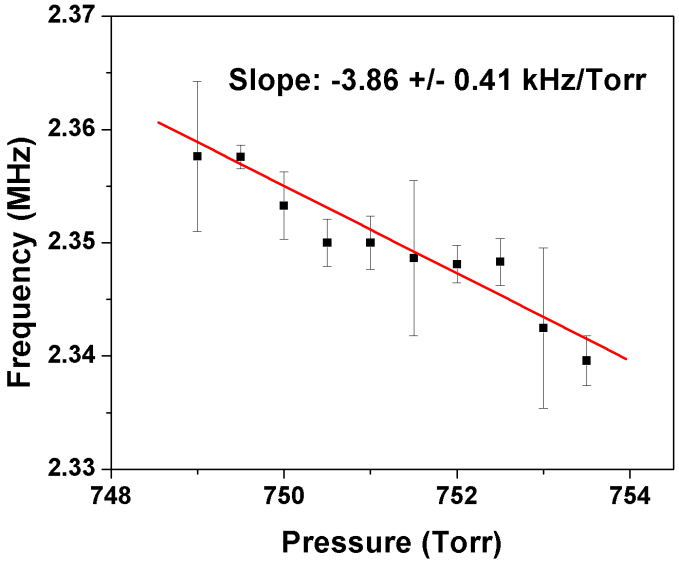

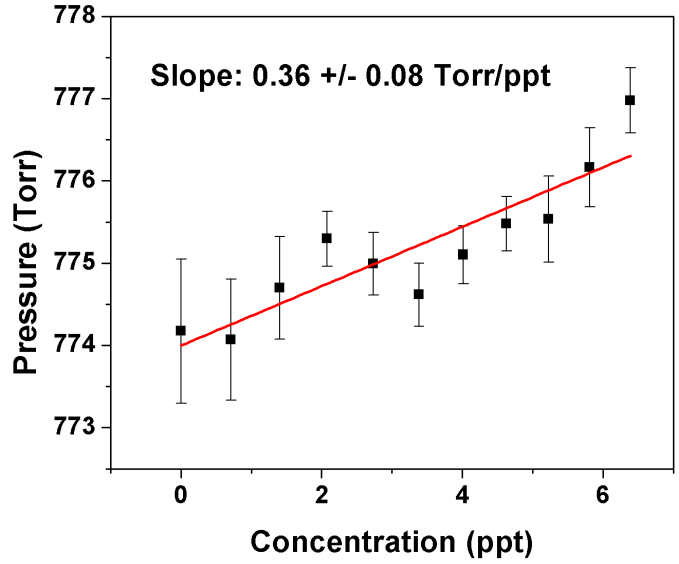

Figure 2.9 (a) Pressure calibration of the RMB in ambient condition ($\Delta f/\Delta P$ = -3.86 ± 0.41 kHz/Torr). (b) Pressure rise per ethanol concentration increase ($\Delta P/\Delta C$ = 0.36 ± 0.08 Torr/ppt)

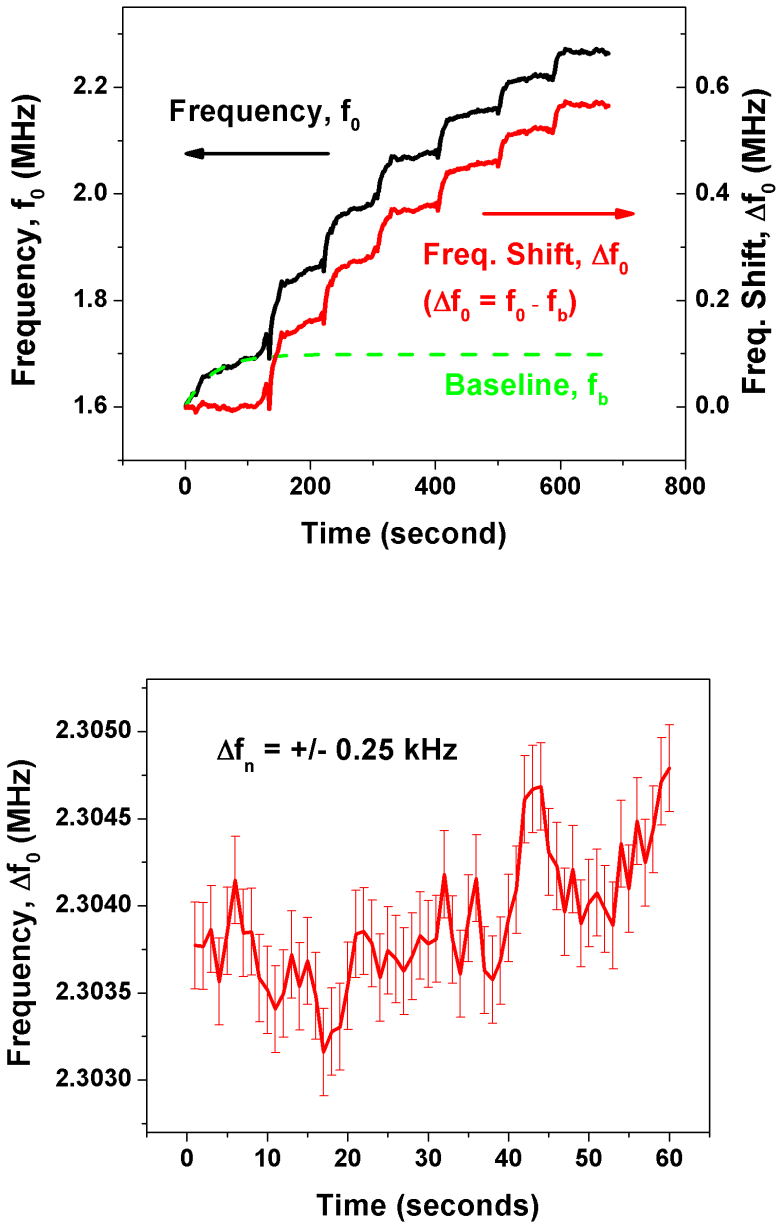

Figure 2.10 (a) Steps of frequency rises upon increase in vapor concentration before and after baseline subtraction (b) Short term frequency noise, Δf_{noise}, or a standard deviation of the frequency fluctuations (Δf_{noise} = ± 0.25 kHz) in a minute

2.5 Frequency Shift Analysis and Device Sensitivity

Thanks to their dynamic range, PMMA coated RMBs can detect the presence of analyte vapors well below their saturated vapor pressure. According to a simplified model[39] of doubly clamped beams under compressive stress, the dependence of the frequency shift on the analyte vapor concentration is approximately

$$\Delta f(C) = \sqrt{\alpha C} \tag{2.4}$$

where Δf is the resonant frequency shift from baseline, C is the concentration of analyte vapor, and α is the analyte-dependent hygrometric expansion coefficient of PMMA. Here we assumed linearity between the strain and the stress of hygrometric expansion in the polymer exposed to vapor. Figure 2.11 demonstrates measured resonant frequency shifts in the functionalized RMB of Figure 2.1 and 2.2 with their fitting graphs for each analyte. These experimental results agree with the theory of dynamics of buckled beams[83,84], showing that the resonant frequency shifts are proportional to the square root of analyte vapor concentration, in the case of the volatile vapors ethanol and benzene. In particular, ethanol showed the highest sensitivity among all analytes for this study. On the other hand, water vapor exhibited weak square-root dependence of resonant frequency shifts with changing concentration. We speculate these observations to partially result from unique complex diffusion mechanism of water in PMMA, which consists of dual mode sorption kinetics present in microvoids due to retarded swelling of the polymer[74].

Similar device characteristics have been observed in other spin coated RMBs, proving a reliable device fabrication scheme (See Figure 2.1). Figure 2.12 shows corresponding measurements of another functionalized RMB, in which the initial buckling is further from the critical buckling state than the RMB tested in Figure 2.11. According to Emam[85], the relieved stress, σ_{rel}, or the difference between the residual stress, $\sigma_{res,}$ and the critical buckling stress, $\sigma_{crit,}$ of a beam structure, is given by (See Eq. (A7) in Appendix))

$$\sigma_{rel} = \sigma_{res} - \sigma_{crit} = \frac{\pi^2 E r^2 q_B^2}{4L^2} \tag{2.5}$$

where q_B is the displacement of the beam in out-of-plane direction. While calculated relieved stress of the critically buckled RMB is ~59.5 MPa that of more buckled RMB is ~113 MPa. This increase in the relieved stress leads to the reduced hygrometric expansion coefficient α measured in all analytes with corresponding ratios. Despite their different initial buckling states, both RMBs exhibit similar behavior of frequency shifts with introduction of vapors, verifying consistent device operations of the RMB.

With these PMMA-coated RMBs, we have demonstrated detection of ethanol vapors in a few hundred ppm range. Figure 2.13 and 2.14 show experimental resonant frequency shifts of the functionalized RMB as a function of time and ethanol concentration in ppm range, respectively. In this regime, dependence of the frequency shift on the analyte vapor concentration effectively becomes linear, yielding $\Delta f/\Delta C_{,ethanol}$ = 360 Hz/ppm to first order approximation after 200 seconds (See Figure

2.14). This value is ~ 250 times greater in magnitude than the frequency shift that results solely due to pressure increase induced by ethanol vapor injection into a flow cell ($\Delta f/\Delta C_{,pressure}$ = -1.39 Hz/ppm calculated results from Figure 2.9 (a) and (b)). As we consider 500 Hz of the short-term resonant frequency noise, corresponding to Figure 2.10(b)), it leads to an estimated minimum detectable concentration of ~1.39 ppm of ethanol vapor (500 Hz / 360 Hz/ppm = 1.39 ppm). With a more sensitive detection scheme than the one used in the current experiment, together with more stable baseline frequencies over time under stabilized conditions, the sensitivity of our RMB could potentially be enhanced significantly below one ppm level.

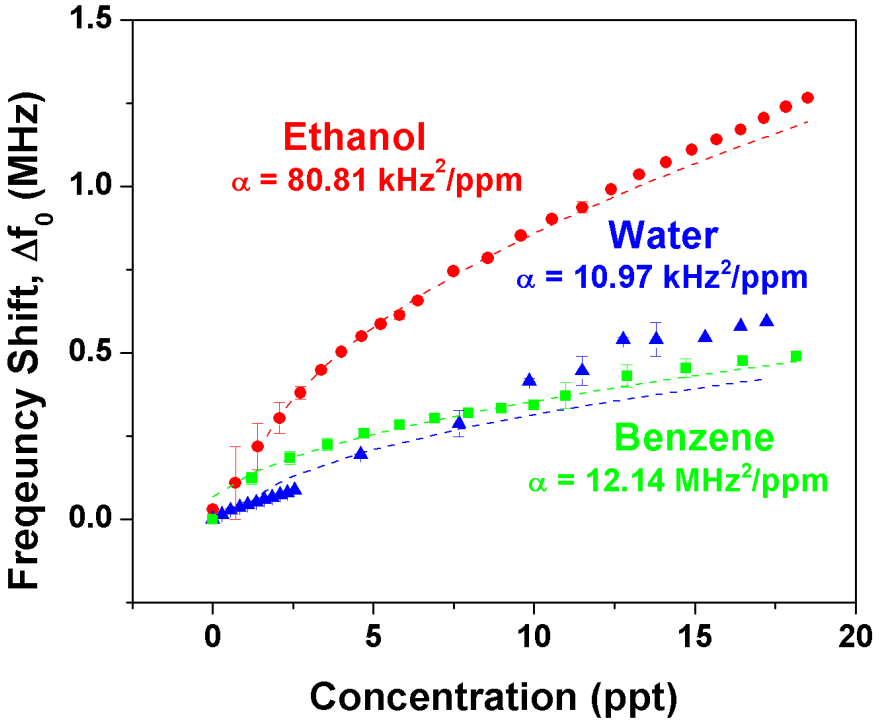

Figure 2.11. Response vs. analyte concentration after its normalization with vapor pressure in a critically buckled RMB (calculated relieved stress = ~72.6 MPa)

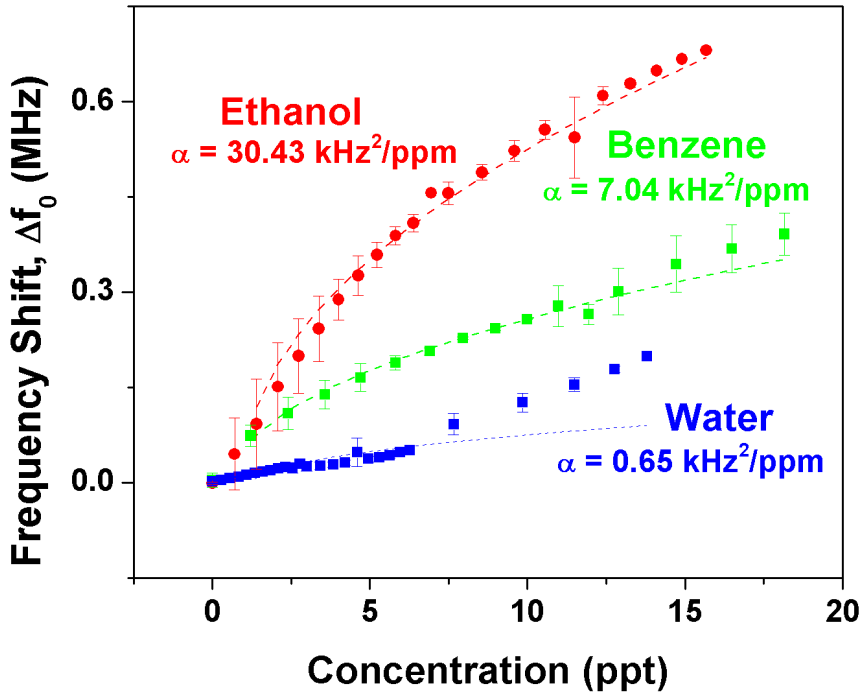

Figure 2.12. Response vs. analyte concentration after its normalization with vapor pressure in a RMB with initial buckling which is further from the critical buckling state (calculated relieved stress = ~138 MPa).

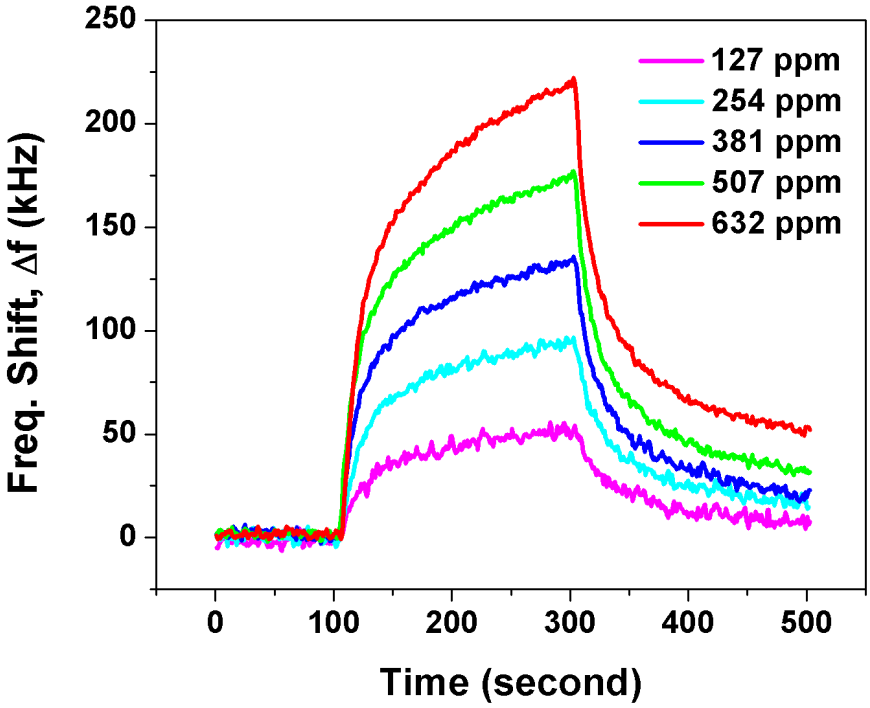

Figure 2.13 Time response of diluted ethanol vapor in ppm range. Response time constant is greater for diluted vapor than saturated vapor

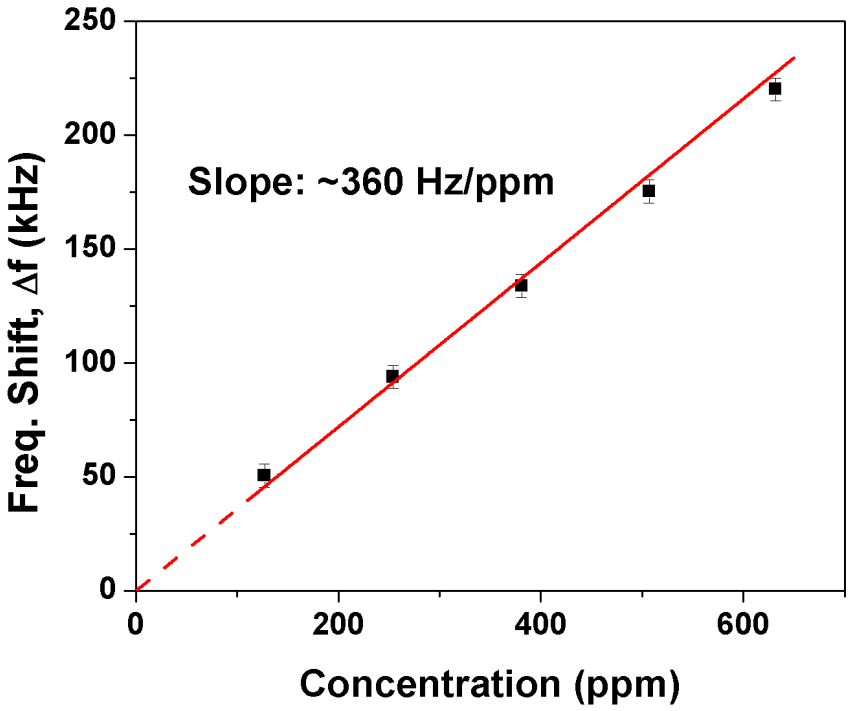

Figure 2.14 Response in frequency shift vs. ethanol concentration in ppm range for the RMB operated near the critical buckling state, 200 seconds after the ethanol injection ($\Delta f/\Delta C_{,ethanol}$ = ~360 Hz/ppm)

2.6 Space-Domain Visualization of Resonant Microbridges

In addition to frequency-domain spectral measurements, dynamics of space-domain vibration profiles (VPs) have also been characterized. VPs in MEMS are traditionally imaged optically with vibrometric[86-88], interferometric[89,90], or stroboscopic[91,92] microscopy. Recently, spatiotemporal evaluations of resonant VPs in high-frequency RMBs have been demonstrated using resonant realtime synchronous imaging (RSI) with a pulsed low duty-cycle nanosecond laser as an implementation of stroboscopic MEMS microscopy[92]. The main feature in RSI is a rapid production of time-resolved interference pattern movies and static profiles, as well as the fast evaluation of VPs, thus supplanting scanned probes that are expensive and inherently slow. This technique is applicable for resonant frequencies up to $f_0 \sim 1$GHz and has shown maximum lateral VP imaging resolution of 250 nm, given high optical contrast. In this work, we use RSI as a tool to study the VPs in RMBs under critical compressive stress as a function of the driving amplitude and ambient pressure. Effects of high drive nonlinearity and damping on the resonator VPs are directly monitored.

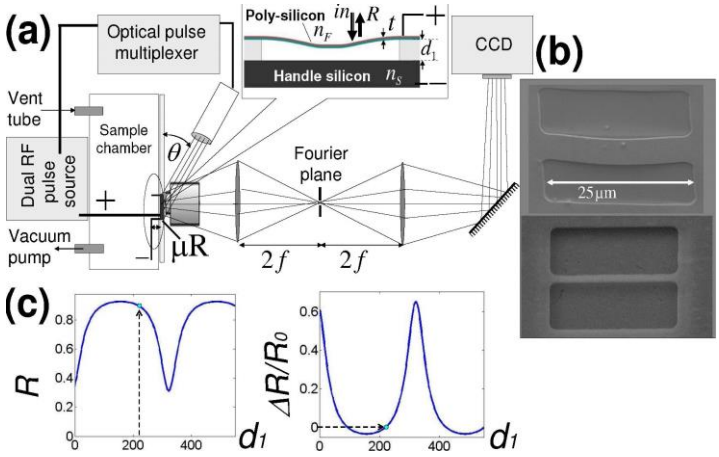

Figure 2.15. (a) Schematics of the experimental setup. (b) SEM images in bridges of dimensions 25×6×0.12 μm^3 (top, slightly buckled) and 20×1×0.14 μm^3 (bottom, flat) and ~220 nm elevations. (c) Calibration curves for synchronous imaging in a device with film thickness t = 138 nm and static midpoint elevation d_0 =220 nm. Left: absolute reflection coefficient R. Right: differential reflection ΔR/R0. A negative value of ΔR corresponds to a negative intensity contrast in the image.

Figure 2.15(a) illustrates a schematic of our RSI configuration. A dual channel pulse source feeds the RMB and optical imaging pulse source multiplexer (Toptica iPulse, λ_0 = 661.5 nm) in synchrony. The collimated illumination at a glancing angle $\theta \approx 45°$ is reflected off the RMB and collected by a microscope objective followed by a 4f lens pair. The latter is used for spatial filtering of the outgoing waveform at the Fourier plane[93]. The light is finally focused on a standard CCD camera at the image plane. Changes in the reflection with respect to the static image of the RMB, due to resonant motion, are monitored as a function of the RF source frequency f_0, voltage and phase. The pressure within the chamber is set with a vacuum pump and venting tubes and read using an auxiliary Pirani gauge above the RMB. In order to calibrate the physical VPs from measured reflection images, an intereferometric analysis is carried out in the out-of-plane direction (inset in Figure 2.15(a)). Applying a 50% duty-cycle to the imaging pulses (full synchronization with the capacitive drive), high inphase sensitivity to average actuation amplitudes is attained at the expense of temporal resolution. Knowing the static film elevation profile d_0, thickness t, the refractive indices of the film nf (n-doped polySi, n=3.916) and substrate nS (single crystal Si, n=3.834), the reflectance coefficient R(x,y) is computed from a Fabry-Perot multilayer analysis in normal incidence, as a function of the total elevation d_1[94]. The measured RSI reflectance R_{meas}, within the CCD dynamic range, corresponds to the differential reflectance with respect to the static RMB profile. This signal corresponds to:

$$R_{meas}(x,y) = \frac{R(x,y) - \mathrm{R}_0}{\mathrm{R}_0} = \frac{\Delta R(x,y)}{\mathrm{R}_0} \tag{2.6}$$

With full sampling synchronization the observed average amplitude <A> at transverse position *(x, y)* is then:

$$\langle A \rangle (x,y) = d_1(x,y) - d_0(x,y) \tag{2.7}$$

Under a periodic unipolar square wave excitation, <A> = $A_{max}/2$, and the glancing angle of illumination (see Figure 2.15(a)) introduces an additional geometric scaling factor cos θ to the apparent amplitude. The actual peak VP amplitudes can thus be deduced from:

$$A_{\max}(x,y) = \frac{2}{\cos\theta}\left[d_1(x,y) - d_0(x,y)\right] \tag{2.8}$$

giving rise to a normalization factor of 2.83 in our implementation. The glancing angle also introduces shadow effects at the edges of the resonator, corresponding to the shadow's changing reflection coefficient during vibration. The latter can be eliminated physically using appropriate phase masks at the Fourier plane, or artificially with post-processing Fourier image analysis. We consider only the reflectance variations at the positions of the RMB itself to constitute its real VPs. An example of total and differential reflectance curves as a function of total elevation d_1, as calculated for a device with thickness t = 138 nm, is shown in Figure 2.15(c). The differential reflectance during motion is taken with respect to the reflectance R_0 at the static mid-

point elevation d_0 = 220 nm. Using Eqs. (2.7) and (2.8), together with the calibration curve, the average and maximum amplitude profiles are estimated. We assume that the film thickness t does not change during the vibrations. Here we will concentrate on characterizations of the fundamental (lowest) resonant mode, even though the method is easily extended to higher harmonics.

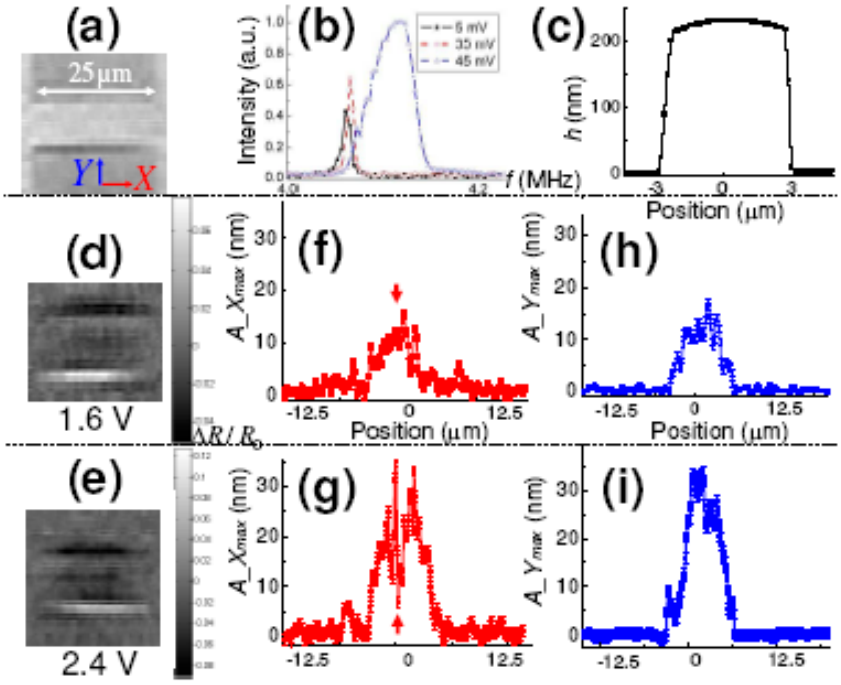

Figure 2.16. Drive amplitude dependence in a nearly buckled resonator's fundamental mode. (a) Reference image of the static bridge. (b) Frequency domain spectra of low-voltage ac actuation voltage under a constant 5V dc bias. (c) Static height profile of the bridge along the Y direction taken from AFM measurements (0 is defined as the height of the trench and known film thickness of 140 nm is subtracted on the bridge). (d),(e) Measured synchronous images at f_0 = 4.1 MHz under different ac amplitudes; (f)-(i) corresponding VPs integrated along Y [in (f),(g) X-profiles], and along X [in (h),(i), Y-profiles].

Figure 2.16 shows studies for a RMB with dimensions ($25\times6\times0.14\ \mu m^3$), and a midpoint elevation gap of 0.22 μm [d_0 = 220 nm and t = 140 nm, corresponding to Figure 2.16(c)], under low pressure settings (P < 1 Torr). The undriven RMB was almost flat (see Figure 2.16(c)) whereas other slightly longer devices exhibit noticeable static upward buckling, suggesting a compressive force whose magnitude is close to the critical load for buckling. Figure 2.16(a) shows the static image of the unactuated device in its initial reference configuration. In Figure 2.16(b) the frequency response under low-voltage actuation is shown. Even with drive amplitudes as low as 45 mV and a dc bias of 5 V we observe the formation of Duffing nonlinearity and significant spectral broadening. An AFM measurement of the static bridge height profile is shown in Figure 2.16(c). RSI images under intermediate and high ac drive voltages, at a frequency corresponding to the maximum resonant amplitude, optimal phase and a dc bias of 5 V, are shown in Figs. 2.16(d) and 2.16(e), respectively. Upon calibration of the amplitudes (using Eqs. (2.6)-(2.8)) and integration across the beam width, the X-profiles (along the length of the beam) are shown in Figs. 2.16(f) and 2.16(g), respectively, and the Y-profiles of motion in Figs. 2.16(h) and 2.16(i). An automated procedure for calibrating each peak amplitude profile requires a processing time of ~2 min and yields reproducible profiles. Under all low and intermediate drive amplitudes the VPs resemble those in Figure 2.16(f) and 2.16(h). Under high drive amplitudes central regions on the beam appear to undergo diminished displacement (Figure 2.16(g)). However, detuning of the imaging frequency in these cases to values near multiples of the fundamental frequency (mostly ~ $2f_0$ and the same phase settings) show some vibrations forming at these locations under these conditions. We

interpret this recurring phenomenon as resulting from either: 1) nonlinear electromechanical processes inducing transfer of energy to higher harmonics at spatial positions of large vibration amplitudes on the RMB, 2) nonlinearity due to the optical response passing at extreme points of the reflection (e.g. see Figure 2.15(b)), or a combination of both of these effects. The exact role could not be discerned unambiguously in the current experiment, but regardless, diminished signal positions such as the one indicated by the vertical arrows in Figure 2.16(f) would clearly not be beneficial to employ for applications of phase-locked-loop (PLL) sensing at this wavelength. Along the Y-profiles, slight localization of the motion at the central region of the bridge is also observed.

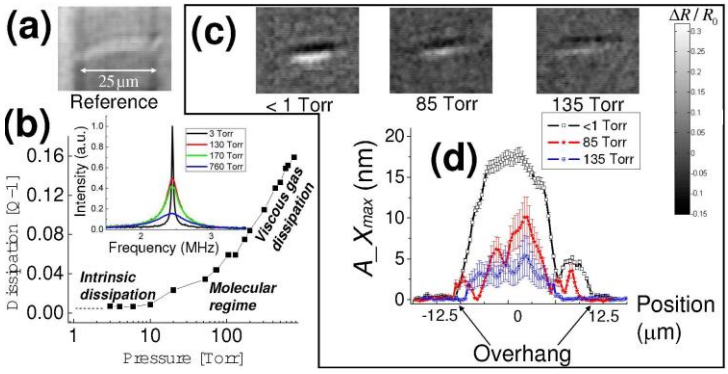

Figure 2.17 Pressure-dependent study in a slightly buckled resonator. (a) Reference image of the static bridge. (b) Frequency domain spectra (inset) and inverse quality factors (dissipation) as a function of ambient chamber pressure, under continuous 315 mV ac drive and a 5 V dc bias. (c) Measured interferometric images at f0 =2.4 MHz as a function of the pressure, and (d) overlayed Y -integrated X -profiles of vibration.

Figure 2.17 shows studies in a narrow microbridge with dimensions ($x \times y \times z = 25 \times 1 \times 0.12\ \mu m^3$) and a midpoint elevation gap of 0.66 μm (i.e., corresponding to d_0 = 660 nm and t = 120 nm in Eqs. (2.6)-(2.8)), under varying ambient pressures and constant driving conditions of 1.2 V ac voltage and 5 V dc bias. This beam was slightly buckled in the upward direction, as observed in the static reference image of Figure 2.17(a). Figure 2.17(b) shows the dissipation (inverse quality factor, Q^{-1}) of the fundamental resonant mode as a function of pressure, and corresponding spectra (inset). Various pressure ranges correspond to different well known dominant dissipation mechanisms[86-88]. In the current experiment we have the ability to record RSI images only at low pressures that are below the viscous (gas-dominated) regime, namely, corresponding to the intrinsic and intermediate molecular regimes. It is estimated that the most significant limiting factors are the low spectral signal-to-noise (S/N) bandwidth at low quality factors (below $Q \sim 50$) combined with diminished amplitudes of motion under external friction. Figure 2.17(c) shows RSI images of the RMB as a function of increasing pressure, with a transition from intrinsic to molecular damping where the SN vanishes. Calibrated maximum amplitude X-profiles, integrated across the beam width (Y), are shown in Figure 2.17(d). A larger error in the VP estimation results from the diminished available RSI S/N that gives rise to larger error in the numerical fits. It is consistently found here, however, that with increasing pressure the VPs become suppressed around the regions corresponding to the bridge overhang (Figure 2.17(d)). This edge suppression effect was not observed in a repeated experiment under low pressure and drive conditions (0.3 V ac voltage and 5 V dc bias), that yield available S/N close to the detection limit, with extracted

vibration amplitudes comparable to the highest pressure case shown here and with noticeable motion near the overhang.

2.7 Conclusion

In summary, we have demonstrated that resonant frequency shifts for PMMA functionalized stress-based resonant volatile gas microsensors, operated near their critically buckled point, can be used in chemical sensing applications. The microsensors exhibit high sensitivity and dynamic range (as large as 150% frequency shifts) enabled by operation near the critical buckling stress with rapid frequency response due to the swelling of the thin polymer coating, effectively increasing surface-to-volume ratio and thus promote faster polymer swelling response. In addition to fast response and high dynamic range, significant improvements in the quality factor of the microsensors in ambient condition were achieved and sensing with the RMB of individual volatile vapors has been demonstrated. The standard microfabrication procedure of doped poly-Si RMBs suggests that the miniaturized microsensors are comparable with electrical detection implemented by complementary metal-oxide-semiconductor (CMOS) based electronics[95] and could be integrated with surface functionalization. Microsensors coated with a high yield functionalization polymer surface can improve their sensitivity, provided that the RMB is pre-stressed closer to its critical buckling. In addition we anticipate that reduction of thermal noise (by use of all-electric detection), and further evolved functionalized coatings will result in higher sensitivity to specific analytes. The mechanism of the stress-optimized doubly clamped beam resonator with surface functionalization is of interest for real-

time volatile-organic-compound ambient gas sensing in applications of breath analysis for trace vapors, biomedical, clinical, and military applications.

CHAPTER 3

ELECTRICAL GRAPHEN SENSOR FOR BIOSENSING

3.1 Introduction

Graphene has its unique physical, optical and electrical properties such as 2-D planar structure, high optical transparency, and high carrier mobility at room temperature. In this study, we describe the use of graphene nanosheets for a novel electrical biosensor. Using a catalyst-free chemical vapor deposition (CVD) method[65,66], the graphene film is grown on a sapphire substrate, confirmed to be a single or a few sheets by Raman spectroscopy and atomic force microscopy (AFM). Simple electrical graphene biosensors are fabricated using traditional microfabrication technology to detect large-sized bio-species such as cancer cells. Human colorectal carcinoma HCT116 cells are sensed through impedance change of an active bio-functionalized graphene device as the cells are captured by immobilized antibodies on the device surface. The functionalized sensors show increase in impedance as large as ~20% of the baseline with a small number of captured cells. This study suggests that the bio-functionalized electrical graphene sensor on sapphire, which is a highly transparent material, is a promising technology to monitor cellular electrical behavior while allowing simultaneous fluorescence-based bioasssays.

3.2 Fabrication and Experimental Methods for Graphene Biosensors

The graphene biosensors are fabricated (mostly in CNF cleanroom) using CVD grown graphene film on sapphire. Alignment marks are first patterned and etched

using RF oxygen plasma for about a minute and RIE aluminum oxide etch for about an hour to etch graphene and sapphire, respectively. Afterwards we pattern the graphene film and briefly apply RF oxgen plasma etch again to define active regions of the sensors. The active graphene channels are 100 μm long and 10 or 20 μm wide. To form drain and source metal contacts, approximately 10 nm thick titanium and 200 nm thick gold are deposited onto both ends of the patterned graphene region by an electron-gun evaporator. A schematic of our fabrication process is illustrated in Figure 3.1.

As shown in Figure 3.2, the bio-functionalization of CVD-grown graphene surface prior to antibody immobilization is performed in the following order: (a) MPTMS is deposited onto the graphene region using MVD in order to create a thiol terminated surface. (b) GMBS solution is applied to the MPTMS-functionalized surface with 30 minutes of incubation and washed with ethanol to generate NHS terminated surface. (c) NeutrAvidin dissolved in 1x PBS is prepared for the subsequent functionalization step and 1 hour incubation is allowed, followed by the PBS wash. And (d) biotinylated EpCAM antibody (Cat. #, BAF960, R&D Systems) is introduced to the NeutrAvidin-functionalized surface. Its concentration is at 15 μm/ml dissolved in 1x PBS with 1% (w/v) BSA (bovine serum albumin) and 0.01% (w/v) sodium azide. BSA and sodium azide are used to prevent non-specific hydrophobic binding and to preserve the antibodies longer, respectively. The antibody-coated surface is washed with 1x PBS after1 hour of incubation in order to remove any excess EpCAM (Epithelial Cell Adhesion Molecule) antibody.

Human colorectal carcinoma HCT116 cells are cultured in McCoy's 5A (Life Technologies) with 10% FBS (fetal bovine serum) and 1% P/S (penicillin-streptomycin) solution. The cells are washed with 1x PBS, trypsinized to be detached from the plate, and collected in a centrifuge tube. After the cells (~ 1×10^6 cells per ml) are suspended, 4% PFA (paraformaldehyde) is applied in the tube on nice for 10 minutes to fix the cells. Subsequently, the cells are washed with 1x PBS and re-suspended with 1x PBS containing 1% (w/v) BSA and 2mM EDTA solution. After the cells, the analyte for this study, are added onto the EpCAM antibody-coated surface, the device is incubated for 1 hour to allow antibody-cell binding interaction and washed with 1x PBS to remove excess cells.

In order to measure its electrical characteristics, each electrical biosensor is connected to a commercial precision semiconductor parameter analyzer (Agilent 4165c) using a probe station as shown in Figure 3.3. A DC voltage source is connected between drain and source metal contacts, which is swept from -500 mV to 500 mV with step of 10 mV and DC output current is measured. While measuring electrical characteristics of bio-functionalized devices, a 10 µl drop of PBS is placed on the sensors (See Figure 3.4). HCT116 cells are added using a micropipette and each sensor with captured cells is confirmed through an optical microscope and measured. Data is collected from graphene device prior to functionalization before analyte is dropped and after cells are captured.

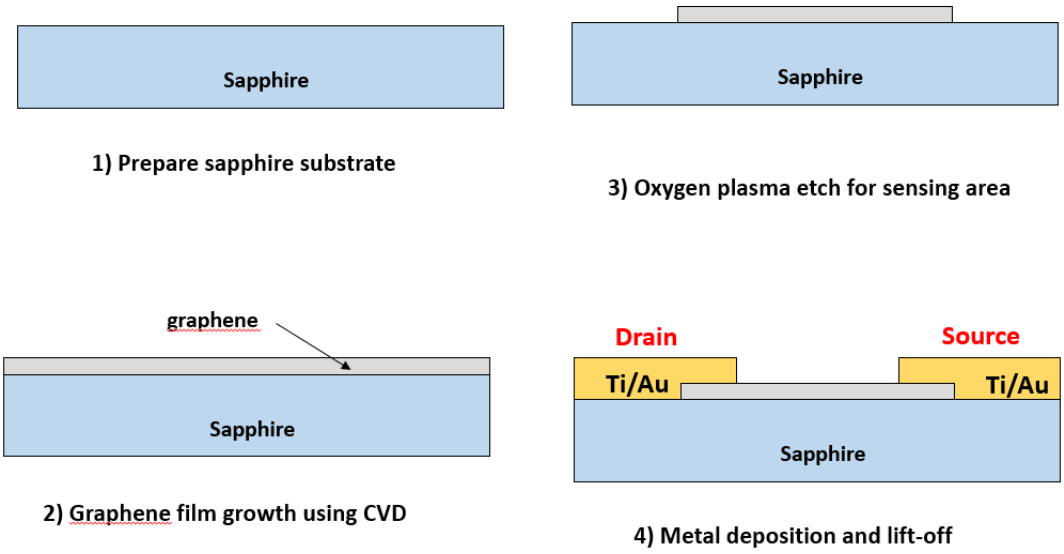

Figure 3.1 Schematic representation of fabrication process of an electrical graphene biosensor prior to the functionalization

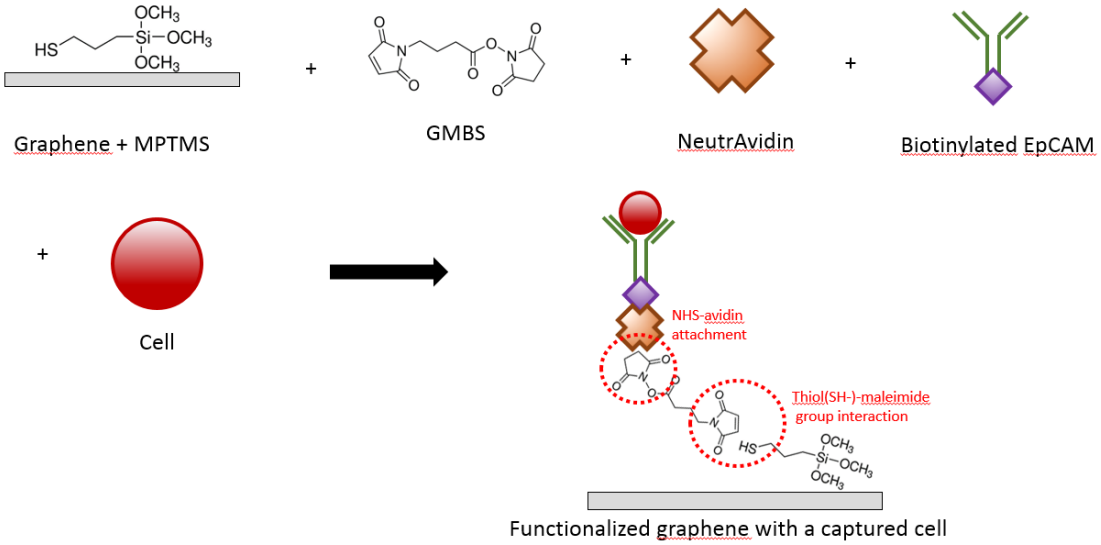

Figure 3.2 Schematic representation of functionalization procedures for the electrical graphene biosensors

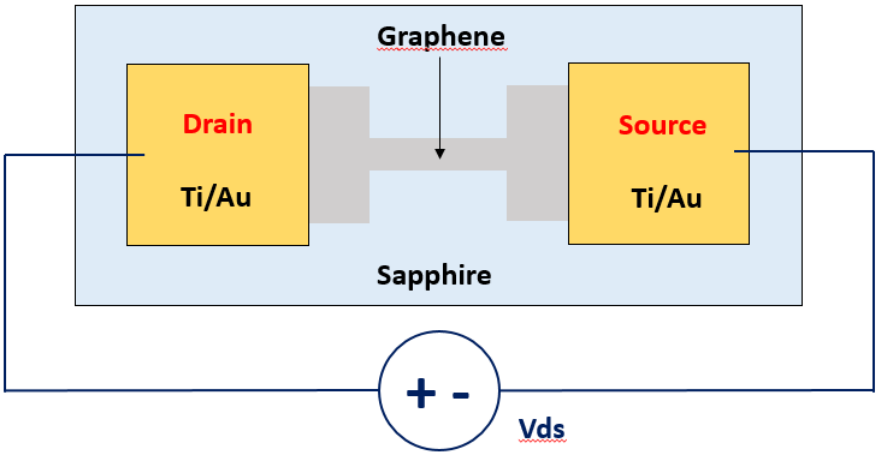

Figure 3.3 Simple schematic of measurement setup prior to graphene surface modification

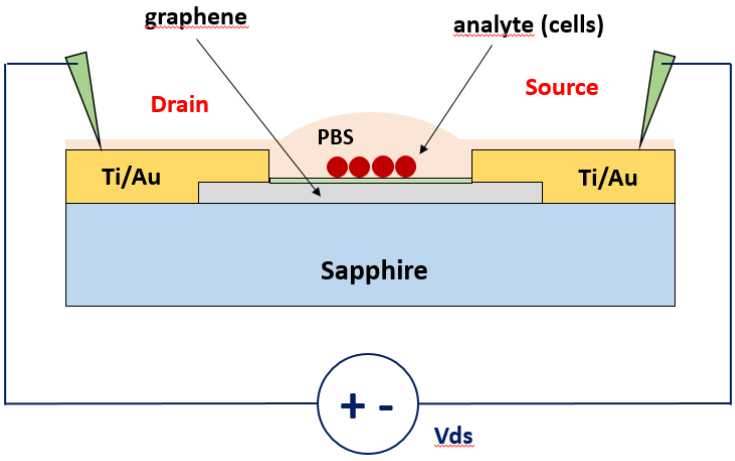

Figure 3.4 Schematic of measurement setup after graphene surface has been modified

3.3 CVD Growth of Graphene on Sapphire

Sapphire, which is inherently transparent, is used as a substrate for electrical insulation of the graphene microsensors. It is also suitable for high temperature graphene growth in order to achieve high-quality graphene nanosheet as it can stay at ~2000 °C. For the growth of graphene, double-sided polished C-plane (001) sapphire substrates are prepared. The substrates are cleaned using acetone and methanol and placed on a graphite carrier to be baked inside a vertical, cold wall and stainless steel CVD chamber (Figure 3.5) at ~600 °C for 30 minutes. Growth temperature is measured and controlled by a pyrometer and a feedback system is raised by a DC electric resistance heater with graphite filaments located at the bottom side of the wafer carrier. Substrate temperature initially increases to be 1000 °C at a rate of 100 °C/min and then reaches its final growth temperature (1350 °C to 1650 °C) at 250 °C/min. Ar, main carrier gas, is introduced into the growth chamber during outgassing with growth rate and set pressure at ~10,000 sccm and 600 Torr, respectively. Methane (CH_4) as a carbon source and hydrogen (both flow rate of 5-15 sccm) are also supplied to the chamber in order to control the growth rate of the graphene film. Typical growth time is as short as 1-5 minutes at higher growth temperature (1550 °C and 1650 °C) and as long as 10-15 minutes for lower growth temperature (1350 °C and 1450 °C). After the growth is completed, sample are immediately cooled down under Ar at a rate of 150 °C/min.

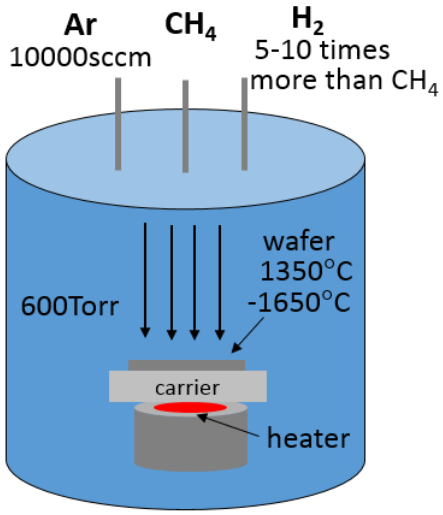

Figure 3.5 Schematic of graphene film growth by chemical vapor deposition (CVD) on sapphire substrate in a chamber

3.4 Characterization: Raman Spectroscopy and Atomic Force Microscopy (AFM)

Raman signatures of graphene are detected from the metal free CVD grown graphene on sapphire as shown in Figure 3.6. G-band from in-plane and 2D-band associated with phonons are observed at ~1600 cm^{-1} and 2700 cm^{-1}, respectively. D-peaks involved in defects are found at ~1350 cm^{-1} and the thickness of graphene is measured, 1 or 2 monolayer (ML) by optical transmission measurements. The intensity ratio between the 2D-peak and G-peak (I2D/IG = ~1.5) in Raman spectroscopy empirically supports the thickness of graphene. Surface morphology of the grown graphene film on sapphire is also examined using AFM as shown in Figure 3.7. It scans the surface over 2 μm x 2 μm and shows smooth surface with the root mean square (rms) roughness of 0.31 nm over the area. The step-like surface features are expected to rist from the sapphire substrate underneath the graphene sheet. There is no wrinkle, fold and grain boundary, which can be easily detected in SiC–based epitaxial graphene.

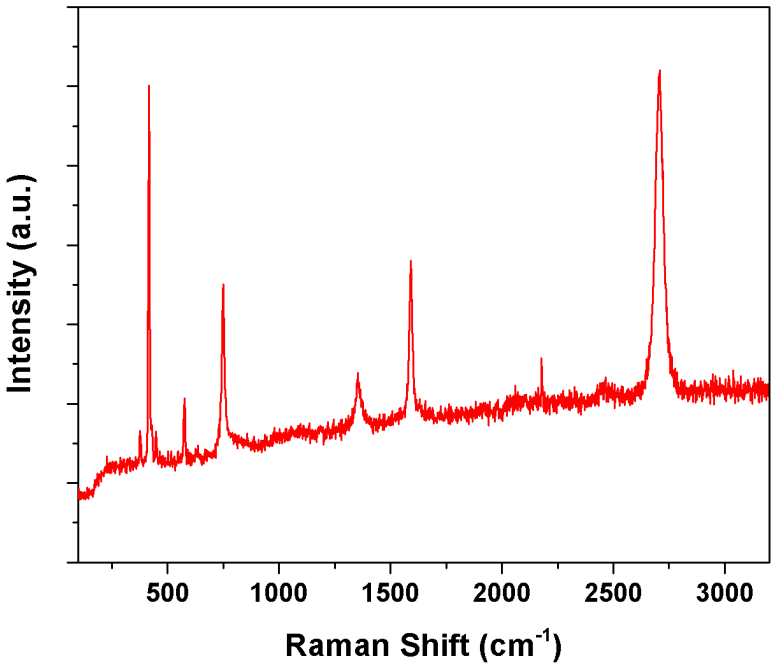

Figure 3.6 Raman spectrum of graphene grown on sapphire

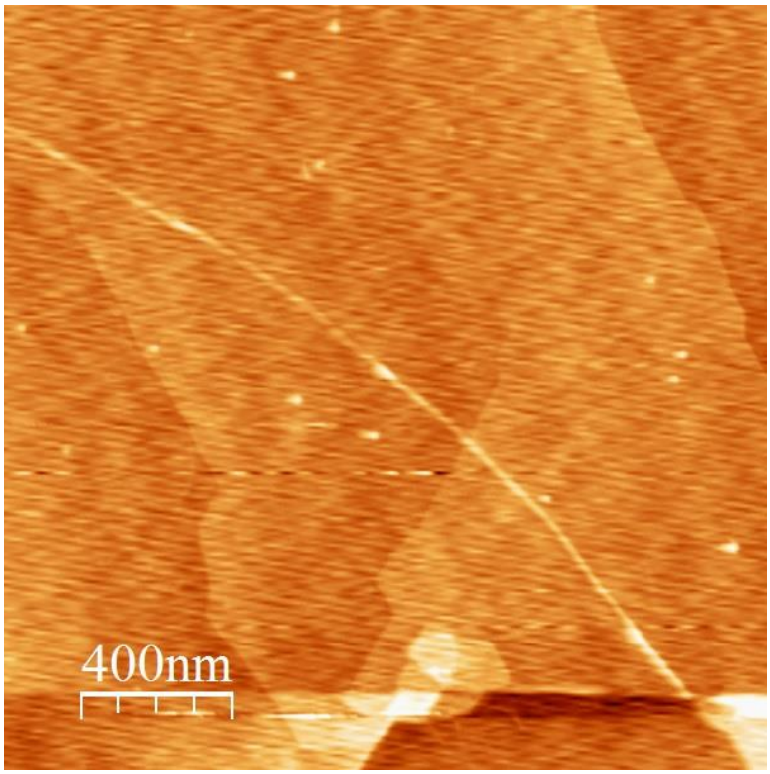

Figure 3.7 AFM image of graphene layer

3.5 Prior to Surface Modification

After we confirm the CVD growth of graphene film on sapphire substrate, electrical biosensors are fabricated using standard photolithography and etch processes. Connecting to a precision parameter analyzer, we measure the electrical characteristics of the graphene biosensor prior to its surface modification at room temperature. A schematic of the electrical measurements is illustrated in Figure 3.3. Drain and source metal contacts of each sensor are connected to a DC voltage source with low voltage bias sweep from -500 mV to 500 mV. Each graphene sensor exhibits a linear relationship between applied DC voltage measured output DC current, confirming each sensor is ohmic. In addition to calculation of output impedance for each sensor, contact resistance between graphene layer and metal contacts is evaluated based on transmission line measurement (TLM). Figure 3.8 shows resistance plotted against TLM gap spacing, or incremental distance between two contact pads ranged from 10 to 120 μm. According to TLM methods, specific contact resistance of ρ_C is calculated as

$$\rho_c = \frac{(\rho_t)^2}{\rho_s} \tag{3.1}$$

where ρ_t is the transfer resistance (half of the y-intersect in Figure 3.8 multiplied by the width of contact pad) and ρ_s is the sheet resistance (slope of the curve in Figure 3.8 multiplied by the width of contact pad) of the graphen layer. Its specific contact

resistance is calculated to be $\rho_C = 4.1 \times 10^{-3}$ (Ω-cm^2) (See Figure 3.8).

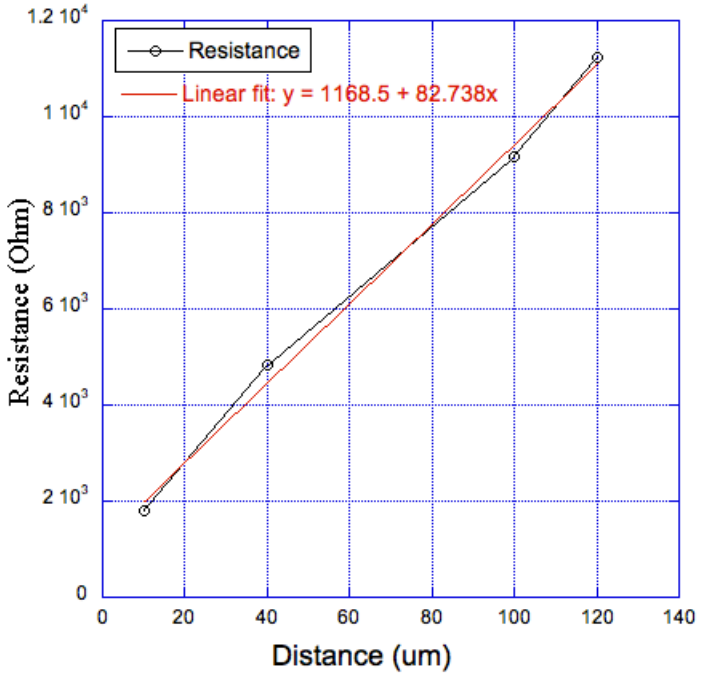

Figure 3.8 contact resistance analysis of graphene device by transmission line measurement (TLM) methods

3.6 Surface Modification

After electrical characteristics of the graphene sensors are measured, we functionalize the surface of graphene active channel, followed by antibody immobilization. Bio-functionalization of graphene film requires several steps as described in Figure 3.2. Similar to its previous electrical characterization, the surface functionalized graphene biosensors are loaded to a probe station and tested with a precision parameter analyzer at room temperature. A cross-sectional illustration of electrical measurements for graphene sensors after surface modification is described in Figure 3.2. DC voltage bias applied between drain source metal contacts is maintained to be no greater than 500 mV, hence keeping a low electrical field to avoid any damages to bio-species. Probe tips are gently connected to both metal contacts as they penetrate through a small drop of PBS buffer solution (~10 µl), which covers the entire functionalized sensor surface. The volume and concentration of the PBS drop are maintained to be the same as the devices are kept at high humidity to prevent evaporation. Neither metal gate electrode nor electrolyte-gate has been implemented for this device configuration, which enables simpler fabrication procedure and experimental setup The leakage current between the solution and the Ti/Au electrodes is measured as the ends of both probe tips are placed inside the PBS solution with a same distance between drain and source metal contacts. It is found to be negligible (less than 30 nA) with the same range of DC voltage bias, as shown in Figure 3.9.

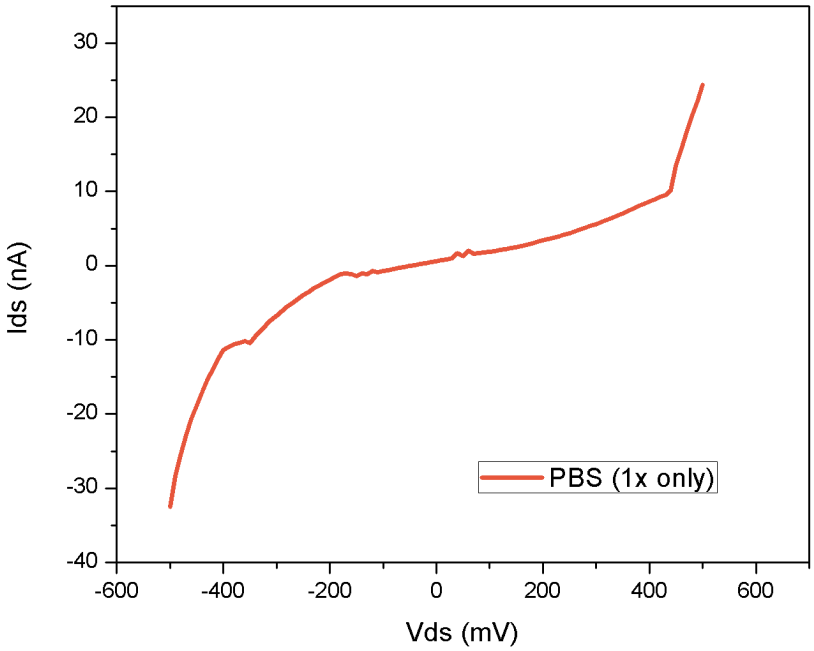

Figure 3.9 Measured leakage current between the solution and the Ti/Au electrodes

3.7 Device Performance

The dependence of electrical impedance of graphene biosensors due to surface functionalization and captured cells is evaluated. Figure 3.10(a) and (b) show optical microscopy images of graphene biosensors array before and after their surface modification followed by immobilization of HCT116 cells. PFA (paraformaldehyde) is applied to fix cells in PBS suspension before they are put on the EpCAM-coated surface. After a period of incubation time (which allows antibody-cell binding interaction) followed by thorough PBS washes to remove excess cells, the electrical dependence of graphene devices is re-characterized. Group of cell clusters were observed as shown in Figure 3.10(b), which caused the electrical impedance of the graphene sensor to increase. The I-V characteristics of the graphene sensor with captured cells are plotted in Figure 3.11, which shows non-linear response between output DC current and the input DC voltage, in contrast to the linear relationship from the bare graphene device (without captured cells) when PBS acgts as the electrolyte. Electrical impedance of graphene biosensor is tabulated in Table 3.1.

Impedance (kΩ)	Graphene Only	After Antibody	After Cell Attachment
With Cell	9.48	16.2	19.3
Without Cell	10.4	18.6	18.7

Table 3.1 Electrical Impedance of Graphene Biosensor

a)

b)

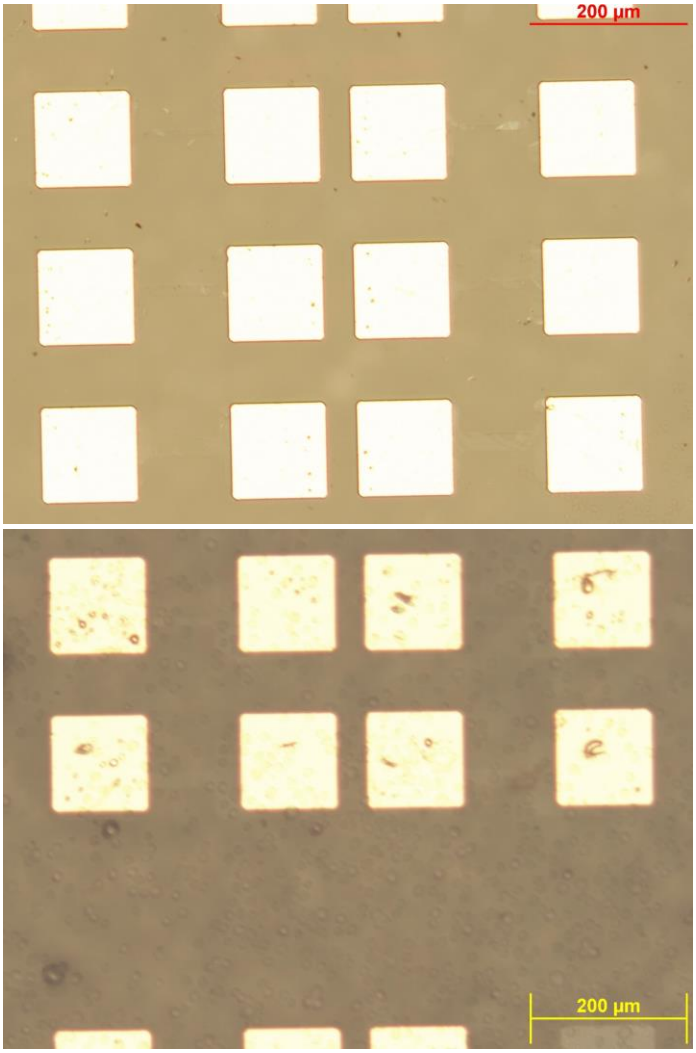

Figure 3.10 Optical microscopy images of graphene sensors a) before b) after surface functionalization followed by antibody and cell immobilization

(a)

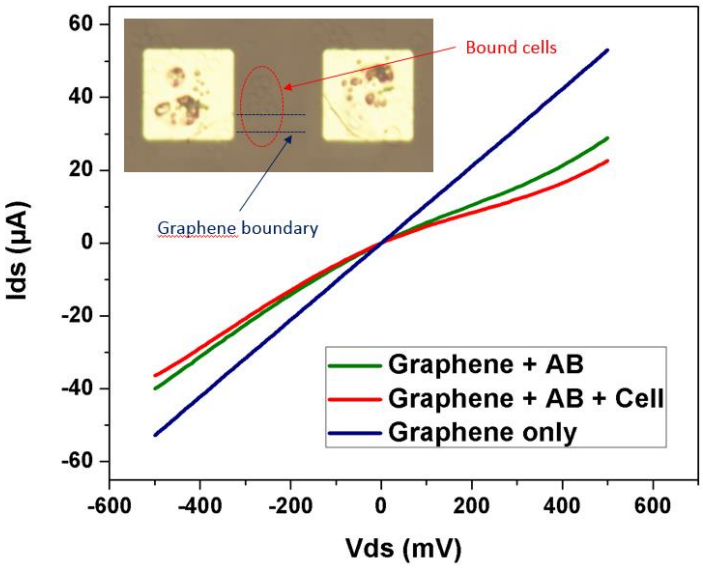

(b)

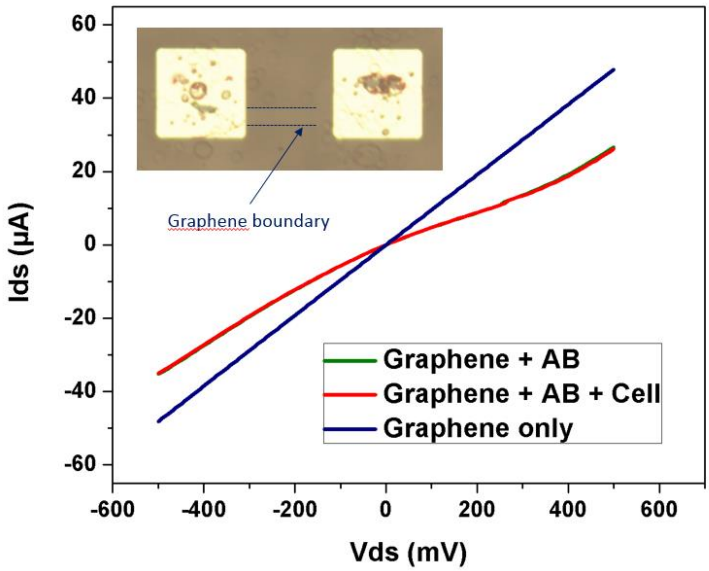

Figure 3.11 I-V characteristics of the graphene biosensor before/after surface functionalization (a) with bound cells (b) without bond cells

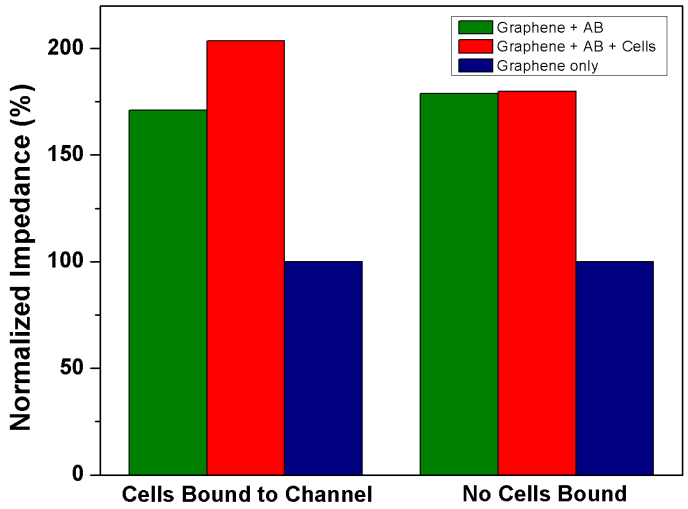

Figure 3.12 Analysis of normalized resistance change

3.8 Further Exploration/Further Consideration

In this work, we have described the use of surface modified electrical biosensors with CVD grown grapheme film. We have demonstrated that cancer cells are sensed through impedance change of the graphene device as large as ~20% of the baseline with a small number of captured cells. However, in order to validate the functionalized electrical grapheme sensor on sapphire as a promising technology to monitor cellular electrical behavior, more sets of experiments are suggested to be performed. First of all, it is needed for the biosensor to be tested with different types of antibodies and other cells as both positive and negative control (e.g. macrophages). It is also suggested that we experimentally verify that the graphene sensors on a sapphire substrate (which is highly transparent) monitor cellular electrical behavior simultaneously with traditional fluorescence-based bioassays (for example, the relationship between cell impedance change and anti-cancer drug dose). Lastly, we may try to improve performance of the sensitivity of biosensors at the level of single-cell sensing.

CHAPTER 4

VISUALIZATION OF METASTATIC CANCER CELLS

4.1 Introduction

Colorectal cancer (CRC) is a leading cause of cancer death worldwide. The most common site of CRC metastasis is the liver[96]. When CRC hepatic metastases are treated with chemotherapy, they almost invariably become chemoresistant. Consequently, five-year survival for metastatic CRC is only ~15% and, despite recent advances, current chemotherapy regimens almost never cure advanced disease.

Genetically engineered mouse models (GEMM) are powerful tools for studying CRC, but they only represent a subset of CRC driver mutations. Human subcutaneous xenograft and orthotopic models in immunodeficient mouse hosts are widely used for mechanistic studies, drug screening, and have provided many critical insights into CRC pathogenesis[97-102]. However, the persistence of poor outcomes among many CRC patients highlights the need for new approaches to complement existing models.

For example, there is currently no robust non-survival surgery requiring model that recapitulates the process of human CRC cell metastasis from the GI tract to the liver, the site of more than 50% of CRC metastases. Another problem is that pre-clinical evaluation of new CRC therapies has a high false-positive success rate[98-101] and there is an urgent medical need for less chemosensitive pre-clinical models to reduce the number of futile CRC clinical trials conducted. A third problem is that human cancer cell studies *in vivo* require immunodeficient mouse hosts to avoid xeno-

immunorejection, a barrier that has limited mechanistic studies of adaptive immunity in CRC progression, tumor vaccines and immunotherapies[101].

To expand the range of pre-clinical human CRC models, we created a resource of mechanistically diverse CRC cell and patient-derived xenograft (PDX) lines that collectively carry the majority of common recurrent somatic CRC mutations, represent all major molecular subtypes and robustly model primary CRCs in the native GI micro-environment via simple tail-vein injection. By controlling the CCR9-CCL25 chemokine axis, these human CRC cells traffic to the GI tract and form orthotopic tumors[103]. This minimally invasive approach avoids potential survival surgery experimental confounders (e.g. needle exit wound tracts, iatrogenic local inflammation and systemic stress), and reduces administrative compliance burden and ethical concerns of surgery associated animal morbidity.

We further develop this resource and demonstrate sequential metastasis of primary human CRC tumors to liver, recapitulating the anatomical route occurring in patients. Finally, we use these hepatic metastases to show that for commonly used anti-CRC therapies such as oxaliplatin, *in vivo* CRC liver metastases have elevated DKK4 levels and upregulated Notch signaling (both of which have previously been associated with CRC chemoresistance)[104,105] and are significantly less chemosensitive vs. paired sub-cutaneous xenografts generated from the same cells.

4.2 Preparation for In Vivo Visualization of Colorectal Cancer Cells in Mice

4.2.1 Two-photon Fluorescence Microscopy

Two photon fluorescence microscopy[106] has revolutionized tissue imaging for medical areas such as physiology, neurobiology, embryology and tissue engineering because it enables deep tissue imaging in live animals[107]. Regular fluorescence imaging involves exciting a fluorophore from the electronic ground state to an excited state by a single photon, for biological applications within the ultraviolet or blue/green spectral range. However, in two-photon microscopy, excitation generated by the simultaneous absorption of two less energetic photons (typically in the infrared spectral range) under sufficiently intense laser illumination[106,107]. This nonlinear process can occur if the sum of the energies of the two photons is greater than the energy gap between the molecule's ground and excited states. Since this process depends on simultaneous absorption of two infrared photons, the probability of two-photon absorption by a fluorescent molecule is a quadratic function of the excitation intensity. Under sufficiently intense excitation, three-photon and higher photon excitation is also possible and deep UV microscopy based on these processes has been developed[106,107].

Two-photon microscopy has a number of advantages over conventional microscopy (such as confocal microscopy) for thick, scattering samples. First, two-photon excitation wavelengths are typically about twice the one-photon excitation wavelengths. This wide separation between excitation and emission spectrum ensures that the excitation light and the Raman scattering can be rejected without filtering out many fluorescence photons. Second, two-photon microscopy is particularly suited for

imaging in optically thick specimens. Near-infrared radiation used in two-photon excitation has orders of magnitude less absorption in biological specimens than UV or blue-green light. The attenuation of excitation light from scattering is also reduced, as the scattering cross-section decreases with increasing wavelength. Third, confocal microscopy uses the emission pinhole aperture to reject out-of-focus light. Inside thick specimens, scattering of the fluorescent photons is inevitable. The resultant path deviation causes a significant loss of these photons at the confocal pinhole. Two-photon microscopy requires no pinhole aperture and minimizes signal loss.

4.2.2 Surgical and Imaging Procedures with 3D Printed Devices

In order to perform *in vivo* real-time imaging metastatic colorectal cancer cells (CRC) in the GI (gastrointestinal) tract of live animal models using two-photon microscopy, we have developed a surgical and imaging platform. First of all, mice injected with RFP-labeled (Red Fluorescence Protein) CRC tumor cells via tail vein are monitored typically for a few weeks. When the size of CRC tumor becomes significant for our purpose of study, the mice are prepared for the surgery and imaging session. At the beginning of the surgery, mice receive an injection of glycopyrrolate, an anticholinergic, intramuscularly at 0.002 mg/100g mouse to assist in keeping the airways clear of fluid build-up. During the surgery all animals are breathing oxygen. All areas to be incised are cleaned and shaved with #40 clippers, cleaned with 70% ethanol, swabbed with proviodine, and numbed with a subcutaneous injection of bupivacaine 0.125% (~0.1 ml). Under anesthesia, we inject fluorescence dyes (typically FITC-Dextran) to the animal to label vasculature and externalize a portion

of the intestine, whose moisture is controlled with saline perfusion. Body temperature is monitored and regulated with a rectal thermometer that controls a heating pad placed under the animal. Using 3D printing methods, we customized coverslips and intestinal supports, which are specifically designed to accommodate our needs for the surgery procedure and imaging microscopy setup. Diameter of a hollow-out cover slip frame is 12 mm, which fits to the 20x water-immersion objective used for the customized imaging setup. 3D printed intestinal stage is designed to contain saline (roughly ~2 ml) while its each edge is smoothened to avoid any tissue damage of mouse small intestine. Schematic mouse with externalized small intestine during surgery and 3D-printing designed cover slip and intestinal support are shown in Figure 4.1(a) and (b), respectively.

While it is under anesthesia, the animal is brought into a custom built two-photon imaging setup[108]. Excitation laser wavelength we used for our experiment is typically 880 nm. A small glass window is put on top of the portion to be imaged (See Figure 4.2). Using the two-photon setup, we first search for CRC tumor location and aim to image cancer and inflammatory cell intravasation, extravasation, vascularization, perfusion and dynamic morphology. The time-lapse images provides direct visual evidence for the evolution of the stem cell niche. The length of an imaging session is typically four hours or less and anesthesia is maintained throughout the procedure. The animal is euthanized imaging with a lethal dose of sodium pentobarbital at the end of a set of the imaging session.

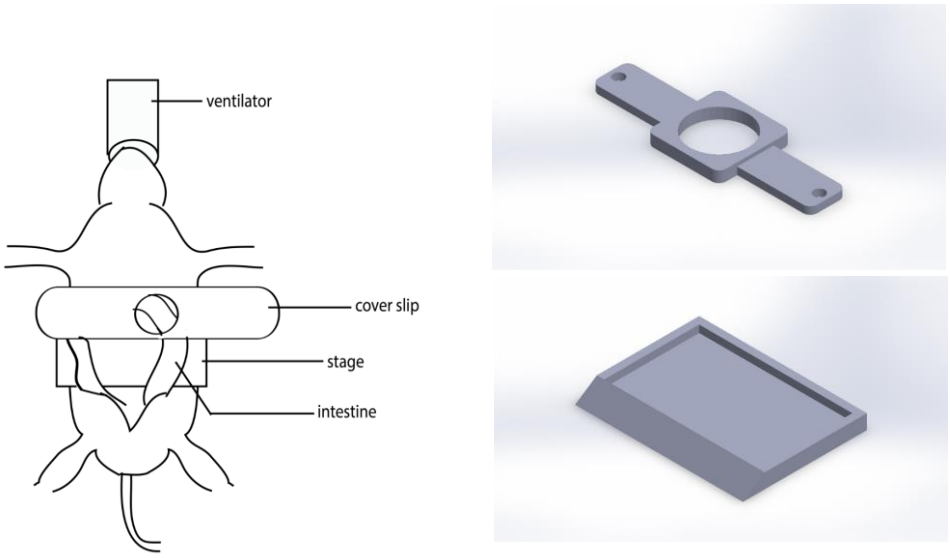

Figure 4.1 (a) Left Simple schematic representation of mouse with externalized small intestine for two-photon fluorescence imaging setup (b) Right: Design of a cover slip and an intestinal support made by a 3D printer

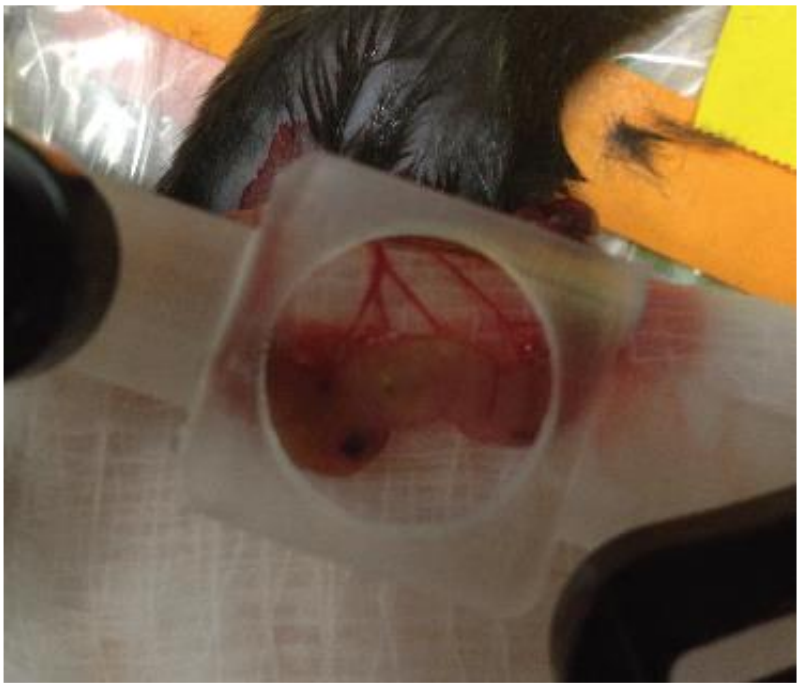

Figure 4.2 Picture of mouse intestine with tumor covered by a glass coverslip on top.

4.3 Modeling Recurrent Human Primary CRC Mutations

Chemokines are secreted ligands that regulate cell trafficking between different organs[109]. Small intestine and colon epithelia produce Chemokine 25 (CCL25), which binds to Chemokine Receptor 9 (CCR9) expressing cells[110-113]. Previously, we reported that CCR9 is up-regulated in primary tumors from early-stage CRC patients, but down regulated in invasive and metastatic CRC tumors. Furthermore, via only mouse tail-vein injection, early-stage CRC cells that endogenously express CCR9 spontaneously form primary CRCs in the colorectum and intestine, attracted by CCL25[96,103].In contrast, blocking the CCL25-CCR9 chemokine axis by short-hairpin RNA (shRNA) or antibodies against CCL25 promotes metastasis and formation of extra-intestinal tumors.

Based on these findings, we established a Chemokine-Targeted Mouse Model (CTMM) system that can be used to study primary human CRC mechanisms of progression and chemoprevention in the native GI microenvironment. Recent genome-wide characterization studies have highlighted the extreme molecular heterogeneity among human CRCs[114]. We therefore systematically generated a panel of 15 doxycycline- inducible CCR9+ cell and PDX lines (See Figure 4.3) to model a diverse spectrum of primary human CRC tumors that carry the majority of common recurrent somatic mutations occurring in patients. This includes not only well-established examples (e.g. *KRAS* and *BRAF*) but also mechanistically poorly characterized recurrently mutated genes such as *ASXL1*,*MLL3* and *LIFR*. Orthogonally, this resource includes multiple examples from all the major histopathological and molecularly

defined CRC sub-types, such as DNA mismatch repair proficient and deficient, CpG Island Methylator Phenotype (CIMP), adenocarcinoma and mucinous sub-types.

To facilitate quantitative experimental monitoring, each model also co-expresses constitutive luciferase and RFP reporters (See Figure 4.3(a)).Using tail-vein injection and luciferase monitoring (See Figure 4.4(a),(b)), within 3 weeks, each CTMM model forms mean 1.88±0.57 colorectal tumors per affected mouse host, (whereas the CCR9- parental lines rarely, if at all, form colorectal tumors (mean 0-0.15)) (Fig. 4.4(c)).

In summary, we have developed a CTMM system to model primary human CRC tumor growth and progression in the native GI microenvironment. This system includes a molecularly diverse resource that spans the majority of recurrent patient CRC somatic mutations. CTMM models can be generated easily within weeks and avoid potential experimental confounding factors from survival surgery implantation (e.g. needle tract exit wounds, iatrogenic local inflammation and systemic stress from anesthesia), as well as reduce administrative compliance burden and ethical concerns of surgery associated animal morbidity. These qualities make CTMM a potentially useful system for evaluation of early-stage CRC progression mechanisms and chemoprevention drug screening.

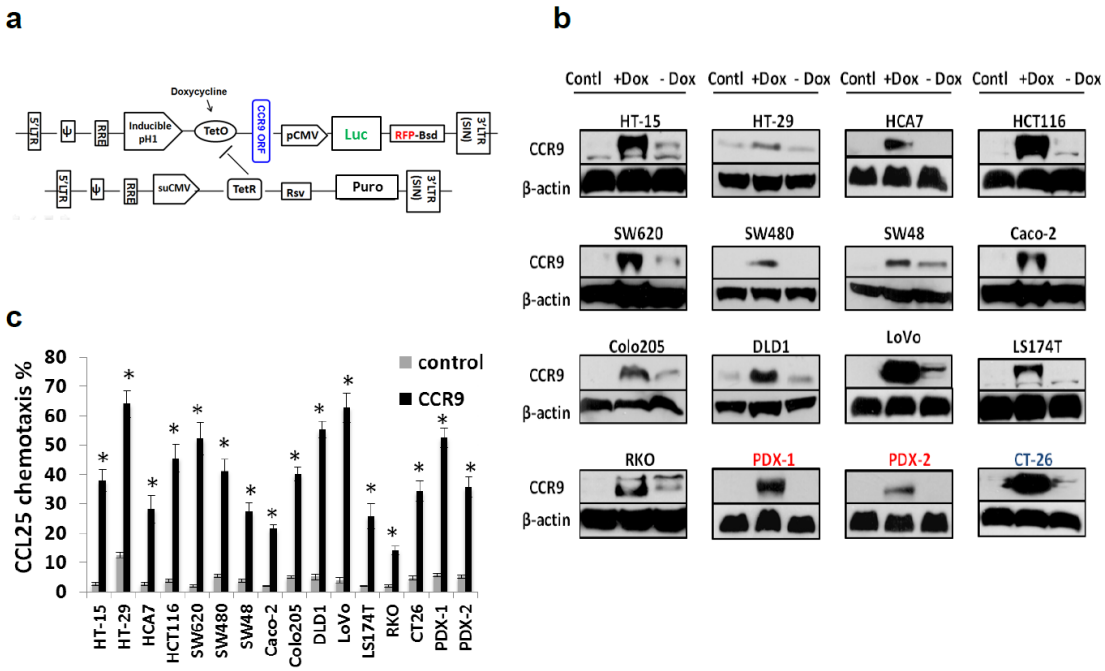

Figure 4.3. Engineering inducible CCR9+ CRC lines and in vitro functionally evaluating the efficiency of CCR9+cells. (a). Schematic of inducible CCR9 expression system which consists of two vectors: the regulatory vector encoding the Tet repressor (TetR) under the control of the human CMV promoter; and an inducible expression vector expressing human CCR9 or mouse Ccr9 genes under the control of CMV promoter and two tetracycline operator 2 (TetO2) sites. This CMV promoter also drives luciferase (Luc) and Red fluorescence protein (RFP) expressions. After packaging the two vectors into lentivirus particles, TetR expression lentivirus was first used to infect common CRC or PDX lines. After puromycin selection, the TetR expressing lines were then infected with the CCR9 inducible expression lentivirus and followed with blasticidin selection and RFP FACS purification. The CCR9 expression can be induced by1-1.5 ug/ml (in vitro) or 1-2mg/ml (in vivo) doxycycline. **(b).** CCR9 protein level expression in parental CRC cells (Ctrl), CRC cells with (+ Doc) or without (- Doc) doxycycine induction were tested by using anti-human CCR9 antibody in western blots.β-actin is loading control.**(c).**In vitro migration of CRC lines toward CCL25 was significantly increased with CCR9 expression, evaluated by Boyden chamber experiments as described in METHOD section. *P< 0.01mean compared to parental CRC cells transfected with control vector by 2-sided MW test.Error bars indicate S.E.M.All cell lines control vs CCR9, P=0.001 2-sided Student t test. (n = 8 each for CCR9+ and CCR9- arm for each cell line analyzed).

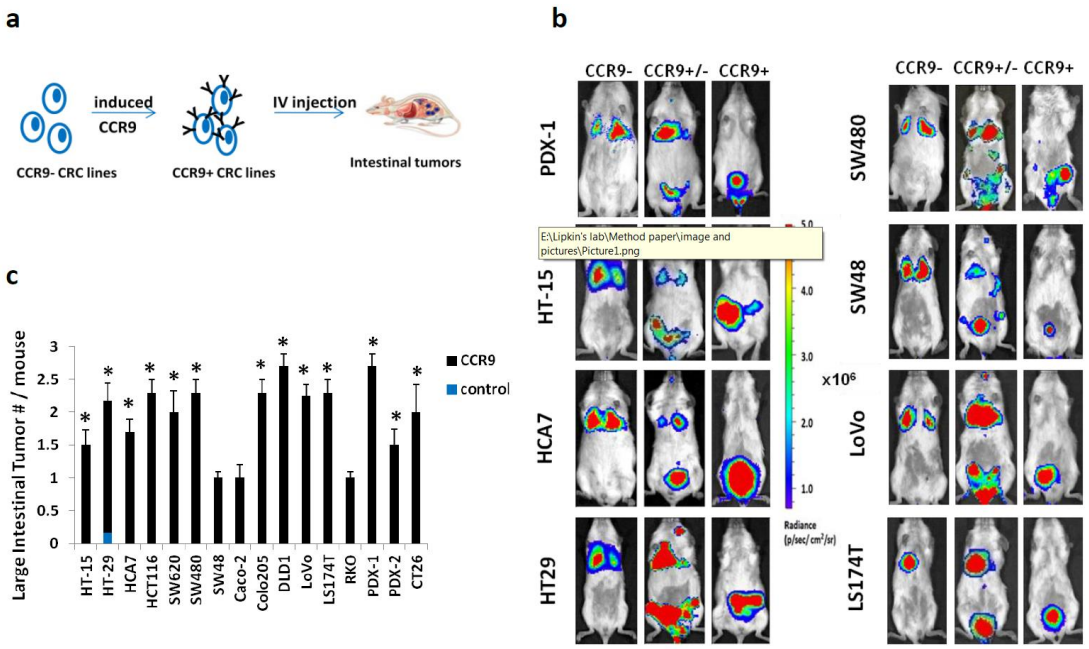

Figure 4.4 Modeling Primary Human CRC Recurrent Mutations in Mice without Survival Surgery (**a**). Schematic of experimental approach: Lentiviral infection with virus containing a Tetracycline inducible CCR9 expression cassette and constitutive luciferase-RFP reporter genes. After puromycin selection and FACS, 0.5-1 x 106 CCR9+ cells were injected into 6-8 week old male or female (m/f) non-obese diabetic/severe combined immunodeficient (NOG) mice by tail vein and intestinal tumor formation monitored after 2-3 weeks by IVIS-luciferase imaging. Blue dots: GI tumors. (**b**). Representative whole body IVIS images of mice injected with CRC cells expressing a control luciferase reporter only (CCR9-), constitutive CCR9 expression and luciferase (CCR9+) or a mixture (CCR9+/-); Luciferase photon signals are shown.(**c**). Quantification of mean luciferase-detectable large intestinal tumors in 6-8 week mice injected with CCR9 expressing cells (CCR9+) via tail vein. * P< 0.01 CCR9+ compared to the control group by 2-sided Mann-Whitney test. Error bars indicate S.E.M. (stand. error of mean). All cell lines combined control vs. CCR9+, P=0.001; Student paired t test.

4.4 Sequential Primary Human CRC-live Metastasis Formation

Seven CTMM models (CCR9-PDX1, HT15, HCA7, SW48, Colo205, DLD1 and LS174T) spontaneously form liver tumors (mean 3.1-8.2 liver tumors/mouse by 8 weeks) but only in mice that have previously developed primary CRCs (See Figure 4.5) IVIS imaging revealed luciferase-detectable primary CRCs (mean 1.8 weeks post-inoculation) preceded liver tumors (mean 5.8 weeks post-inoculation). In contrast, liver tumors were rarely detected in non-CTMM models, in which tail-vein injected CRC cells usually form tumors in the lung (See Figure 4.5).

These findings are potentially consistent with a model whereby CTMM promotes cells from primary CRC tumors to metastasize to liver, most likely via the portal circulation. To test this model, we tail-vein injected mice to generate primary CRC CTMM models. After primary GI tumor formation was detected by IVIS imaging, we next withdrew doxycycline to suppress CCR9 expression. In all CTMM lines tested liver tumor multiplicity was significantly higher when CCR9 levels were suppressed. Additionally, FACS of mouse liver cells 48 hours after tail vein injection of CCR9+ CRC cells showed that RFP+ cells were essentially undetectable arguing against an alternative model in which CCR9 suppression stimulated expansion of previously resident human CRC cells in liver.

Next, to confirm that CTMM primary CRC tumor cells could enter the portal circulation, we injected mice with FITC-Dextran to label vasculature and used Multi-Photon Microscopy (MPM) to image the primary tumor and liver metastatic tumors *in vivo* as we have previously described (See Figure 4.1). This revealed that RFP+ human CTMM cells co-localize with and travel through host blood vessels, consistent

with vascular intravasation (an important step prior to entry into the portal circulation that drains to the liver)**.**

In summary, our data are consistent with a subset of molecularly well-characterized CTMM primary CRC tumors that are capable of sequentially modeling the progression of primary human CRC to liver metastases via the portal circulation that occurs in over 50% of stage IV CRC patients. Furthermore at even later time-points, luciferase+ cells spreading at additional sites such as lung were also observed.

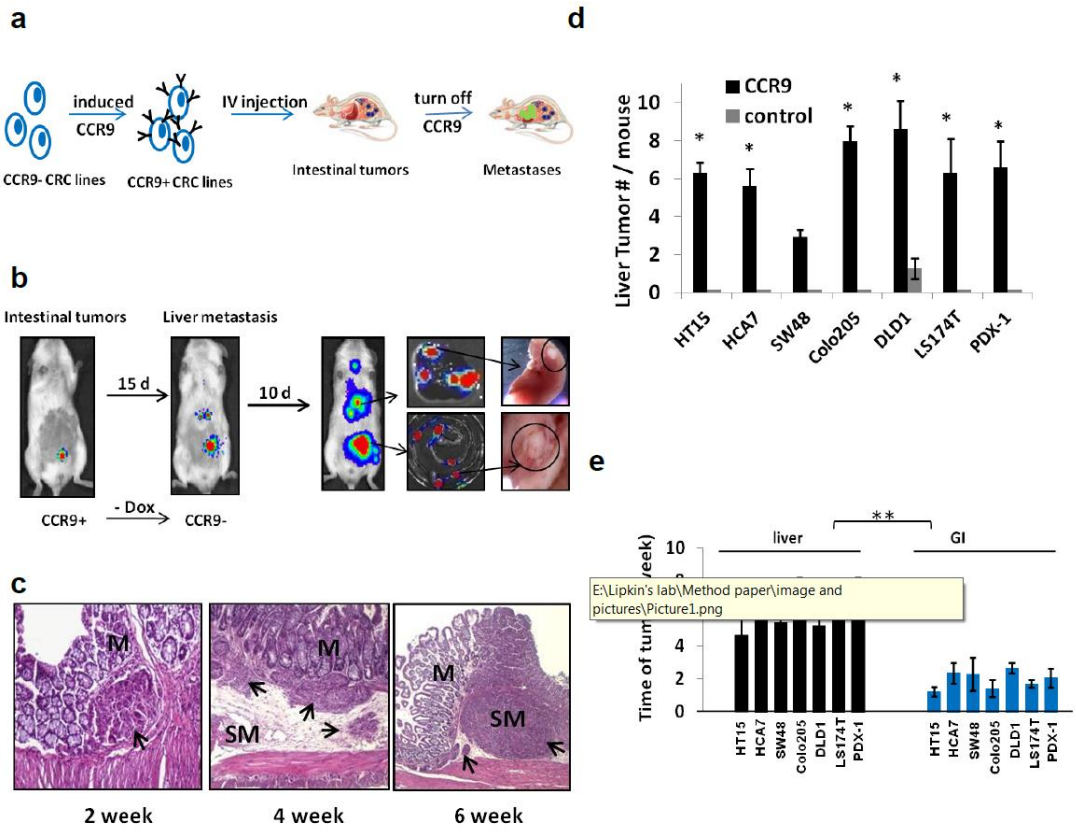

Figure 4.5. Sequential human CRC primary GI tumor- metastasis formation (a). Schematic of sequential human primary CRC and liver metastasis. Using the same approach as in **Figure 4.4,** in 6-8 week m/f NOG mice were injected with CCR9+ human CRC cells and monitored by IVIS imaging for primary CRC formation. Once primary GI tumors were detected, CCR9 expression was silenced by withdrawing doxycycline from drinking water. Mice were monitored using IVIS-luciferase imaging over the next 4-6 weeks and sacrificed. Blue dots: GI tumors; green dots: metastatic tumors. **(b).**Representative whole-body IVIS images(CRC line DLD1 as representative) show sequential lower abdominal and right upper quadrant abdominal detectable photons, with ex vivo confirmation of abdominal right upper quadrant tumors as liver-localized(4X)(n = 8 each for CCR9+ and CCR9- arm for each cell line analyzed).**(c).**Histopathology (H+E staining) examples of different primary CRC tumors detectable as submucosal (2_{nd} week), with invasion of submucosa (4_{th}week)and muscularis(6_{th} week). Arrows indicate histopathologically confirmed tumors; M, mucosa; SM, submucosa. Scale bars, 100μ.**(d).**Quantification of liver metastases in mice (n = 8 each for CCR9+ and CCR9- arm for each cell line analyzed) tail vein injected with control lentiviral vector infected CRC cells (control) or CRC cells with inducible CCR9 expression. * P< 0.05 compared to the control group by 2-sided Mann-Whitney test. All CCR9+ vs. control cell lines, P=0.001 2-sided Student t test. **(e).**Time post-injection of cells with inducible CCR9 expression to luciferase-detectable signal in histopathologically confirmed primary GI or liver tumors (n = 8 mice each for CCR9+ and CCR9- arm for each cell line analyzed). ** P< 0.01 by 2-sided Mann-Whitney test. All cell lines liver vs. GI tumors, P=0.001 2-sided Student t test.

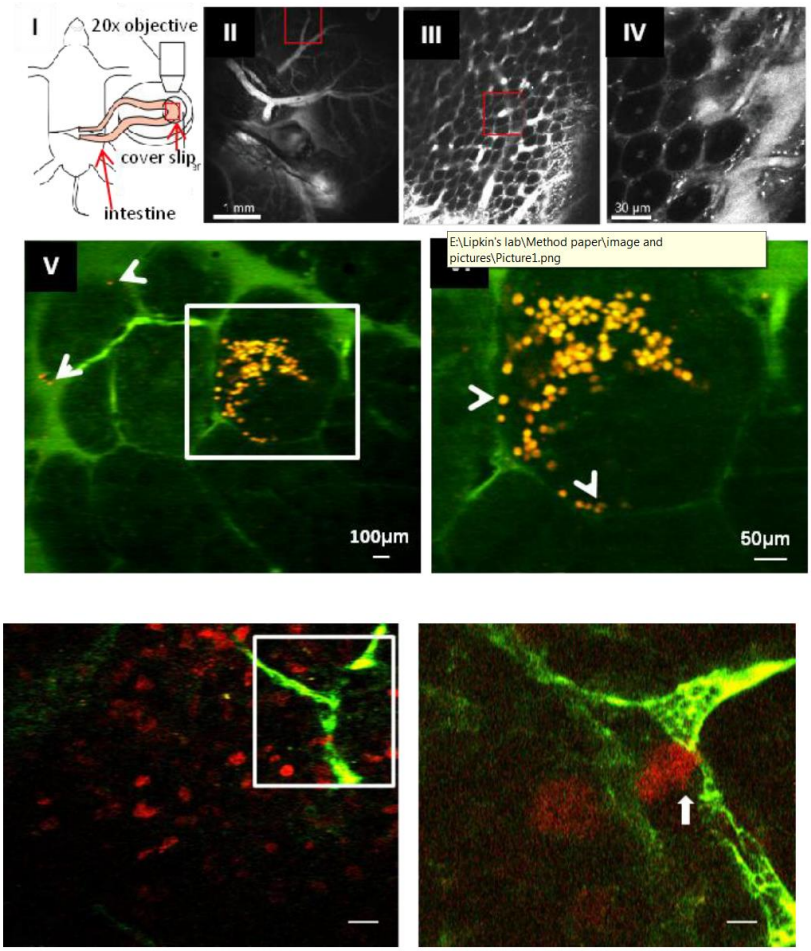

Figure 4.6.Two-photon microscopy imaging of hepatic metastatic tumors
The experiment procedure to form primary CRC and sequential liver metastases was described in **Figure 4.5. (a).**two-photon microscopy imaging of orthotopicxenograft tumors. (representative images on tumors formed with CCR9+ DLD1 cells) (I. Schematic of surgical and imaging preparation (also referred in METHOD part); II – IV. low magnificence images of intestine; V – VI. High magnificence imaging of intestinal tumors expressing RFP (red) surrounding vasculature labeled by FITC-Dextran (green).White arrows designate intravasating tumor cells.)**(b).**(Representative images on liver tumors formed with DLD1 cells)Hepatic tumor cells expressing RFP (red) surrounding vasculature labeled by FITC-Dextran (green).White arrows designate extravasating tumor cells out of blood vessel.) Scale bars, 50µ (left) & 10µ (right). N=6 mice were examined.

4.5 Discussion

Recent comprehensive molecular studies such as TCGA have provided a broad range of insights with an unprecedented level of molecular resolution into the precise molecular alterations that drive human CRC pathogenesis and progression. However, new pre-clinical models are needed to augment existing ones and recapitulate more fully the diverse nature of both cell-autonomous signaling pathways and non-cell autonomous interactions between tumor cells and their orthotopic primary, metastasis-route and -destination site microenvironments.

Towards this goal, we systematically generated a resource of human primary CRC CTMM models that collectively carry the major recurrent somatic alterations occurring in CRC patients. This can be used to study the mechanistic role of the majority of recurrent human CRC mutations multi-dimensionally. In order to confirm the model, we used *in vivo* real-time two-photon microscopy to image primary and liver metastatic tumors. We successfully imaged fluorescently labeled intravastating and extravasating tumor cells along with surrounding vasculature (See Figure 4.6), which is direct visual evidence of the tumor cells that metastasize through the vasculature.

With regard to modeling primary CRC tumor progression, current hepatic metastasis models using human CRC cells are time- and labor-intensive and technically challenging, which limits their usage for drug development. Direct injection of human CRC cells into the heart left ventricle, kidney capsule or spleen are potentially confounded by anatomical routes to the liver that do not recapitulate the microenvironment favorable for transit from the gut through the portal circulation and

lymphatics that occur in almost all advanced stage CRC patients[96]. The portal circulation is known to have distinct features that distinguish its microenvironment from other vasculature. For example, hepatic vein, lymphatic and tributary flow to the liver is unique in that it receives both oxygenated and deoxygenated blood (the latter from gut) and consequently has lower pO2 and hemodynamic perfusion pressure than other organs[115-117]. Furthermore, hypoxia can promote metastasis in multiple types of cancer[118-123]. Therefore, it is highly likely that not only GI microenvironment pre-conditioning from interactions with colon myofibroblasts, dendritic cells, the gut microbiome and native intestinal extracellular matrix impacts CRC liver metastasis, but also pre-conditioning by the portal circulation microenvironment as well.

In summary, we anticipate that the CTMM resources described here can help improve our mechanistic understanding of primary CRC-microenvironment interactions (particularly those involving adaptive immunity and immunotherapies), liver metastasis pre-conditioning by transit through the portal circulation, and potentially improve the clinical relevance of pre-clinical anti-CRC drug screening.

CHAPTER 5

CONCLUSION AND FUTURE WORK

The work presented in this dissertation has discussed characteristics, and utility of microdevices for sensing applications. We have shown several achievements that include development of micro fabrication techniques for mechanical and electrical sensing devices and demonstration of chemical vapor sening in ambient condition using critically buckled functionalized resonant microbriges and detection of cancer cells using electrical graphene biosensor. In latter part of this work, we presented visualization of metastatic colorectal cancer cells using multi-photon microscopy based on genetically engineered mouse models (GEMM). However, there is still substantial room for improving the utility of microsensors and which will hopefully be addressed in the future. For example, the surface functionalized gas microsensors may be constructed as a series of an array where each critically buckled microbridge is coated with different polymer. We anticipate that this will enable selective sensing of individual volatile vapors with high sensitivity, which can be used in applications of breath analysis for trace vapors, biomedical, clinical, and military applications. There is still plenty room for improvement of surface modified electrical graphene biosensors on sapphire in terms of testing different antibodies and cells (or even different bio-species such as DNA or protein) and of verification of sensor usage simultaneously with traditional fluorescence-based bioassays. We expect that it can become a promising technology to monitor cellular electrical behavior.

APPENDIX A: DERIVATION OF FUNDAMENTAL FREQUENCY OF A BUCKED BEAM

In order to highlight the main ideas beyond the operational principle of the sensor, we first consider the resonant behavior of the pre-buckled beam and, specifically, the influence of the axial compressive force on the fundamental frequency of the device. The dynamics of free undamped vibrations of the beam, considered in the framework of the Euler-Bernoulli theory, are governed by the equation

$$EI\frac{\partial^4\hat{z}}{\partial\hat{x}^4}+\left[\hat{P}-\frac{EA}{2L}\int_0^L\left(\frac{\partial\hat{z}}{\partial\hat{x}}\right)^2\right]\frac{\partial^2\hat{z}}{\partial\hat{x}^2}+m\frac{\partial^2\hat{z}}{\partial\hat{t}^2}=0 \qquad \text{(A1)}$$

Here $\hat{z}\ \hat{x},\hat{t}$ is the deflection of the beam (the elevation with respect to its straight stress-free state), $\hat{x}$ and $\hat{t}$ are the coordinate along the beam and time, respectively, L is the length of the beam, m is the mass per unit length, E is the Young's modulus. In addition, I and A are the second moment of the cross-section and the cross-sectional area, respectively. The equation (A1) is completed by the boundary conditions corresponding to the fixed (in both x and z directions) ends of the beam. The non-dimensional, more convenient for the analysis, counterpart of Eq. (S1)[83] is

$$z^{IV}+\left[4\pi^2P-\frac{1}{2}\int_0^L z'^{\,2}\right]z''+\ddot{z}=0 \qquad \text{(A2)}$$

Here

$$z=\frac{z}{r},\quad x=\frac{\hat{x}}{L},\quad t=\hat{t}\sqrt{\frac{EI}{mL^4}},\quad P=\frac{PL^2}{4\pi^2 EI},\quad r=\sqrt{\frac{I}{A}} \tag{A3}$$

One observes that the deflection of the beam is normalized by the gyration radius r of the cross-section and the compressive axial force is normalized by the Euler's buckling force of a double-clamed beam $P_E=4\pi^2 EI/L^2$.

Note that the natural frequencies and natural modes of the beam pre-buckled by the force $P>1$were analyzed in Nayfeh *et al.*[83]. However, the exact characteristic equation used for the calculation of the natural frequencies is cumbersome and difficult for analysis. Here we present a simple, based on the Galerkin decomposition, approximation allowing estimation of the frequency and illustrating the influence of the axial stress on the spectral characteristics of the beam. Since $P>1$, we represent the elevation of the beam in the form

$$z\ x,t\ =z_B\ x\ +w\ x,t \tag{A4}$$

where $z_B\ x$ represents the buckled shape of the beam and $w\ x,t$ is the deflection with respect to the buckled shape. We substitute (A4) into (A2), linearize the resulting equation for $\max_{x\in 0,1}(w)\ll 1$and, taking into account that $z\ x\ =z_B\ x$ satisfies the static counterpart of Eq. (A2), we obtain

$$w^{IV}+\left[4\pi^2 P-\frac{1}{2}\int_0^1 z_B'^{\,2}\right]w''-\left(\int_0^1 z_B' w' dx\right)z_B''+\ddot{w}=0 \tag{A5}$$

In the framework of the single degree of freedom approximation, we set

$$z_B\ x\ \approx q_B\phi\ x\ ,\quad w\ x,t\ \approx q\psi\ x\ e^{i\omega t} \tag{A6}$$

Here $\phi\ x\ =\left[1-\cos\ 2\pi x\ \right]/2$ is the first buckling mode of the beam and[83]

$$q_B = 4\sqrt{P-1} \tag{A7}$$

is the midpoint elevation of the beam in the post-buckled configuration. Substituting Eq. (A6) into (A5), multiplying it by $\psi\ x$, integrating by parts and taking into account fixed boundary conditions yields the eigenvalue problem

$$\left\{\int_0^1 \psi''^{\,2}dx-\left[4\pi^2 P-\frac{1}{2}q_B^2\int_0^1 \phi'^{\,2}dx\right]\int_0^1 \psi'^{\,2}dx+q_B^2\int_0^1\phi'\psi'dx\int_0^1\phi'\psi'dx-\omega_1^2\int_0^1 \psi^{\,2}dx\right\}q=0$$

The lowest natural frequency of the buckled beam is therefore given by the expression

$$\omega_1=\sqrt{\frac{\int_0^1 \psi''^{\,2}dx-4\pi^2 P\int_0^1 \psi'^{\,2}dx+q_B^2\left[\frac{1}{2}\int_0^1 \phi'^{\,2}dx\int_0^1 \psi'^{\,2}dx+\left(\int_0^1\phi'\psi'dx\right)^2\right]}{\int_0^1 \psi^{\,2}dx}} \tag{A8}$$

We use the first buckling mode of the beam as the base function, i.e.,

$$\psi\ x\ =\phi\ x\ =\frac{1}{2}\left[1-\cos\ 2\pi x\ \right] \tag{A9}$$

and obtain

$$\omega_1=\sqrt{\frac{b-4\pi^2 Ps+\frac{3}{2}s^2q_B^2}{a}}=\omega_1^0\sqrt{1-4\pi^2 P\frac{s}{b}+\frac{3}{2}\frac{s^2}{b}q_B^2} \tag{A10}$$

where the coefficients

$$b=\int_0^1 \phi''^{\,2}dx=2\pi^4,\quad s=\int_0^1 \phi'^{\,2}dx=\frac{\pi^2}{2},\quad a=\int_0^1 \phi^2 dx=\frac{3}{8} \tag{A11}$$

are associated with the bending, stretching stiffness and the mass, respectively and $\omega_1^0=\sqrt{b/a}=4\pi^2/\sqrt{3}$ is the (Rayleight quotient) approximation of the fundamental mode frequency of the beam without an axial force. Note that ω_1^0=22.792 while the exact value is 4.73^2=22.373. Substituting (A11) into (A10) and taking into account the expression for q_B, Eq. (A7), we obtain

$$\omega_1=\omega_1^0\sqrt{2\ P-1} \tag{A12}$$

or, taking into account Eq. (A7)

$$\omega_1=\frac{\omega_1^0 q_B}{2\sqrt{2}} \tag{A13}$$

Equation (A13) indicates that in the framework of the single mode approximation the frequency of the buckled beam is a linear function of the midpoint elevation of the beam. Comparison between Eq. (A12) and the exact result given in Nayfeh *et al.*[83] shows that the relative error in the frequency is 4.8% for P=2 (which corresponds to q_B=4 or to the midpoint deflection to the thickness ratio of $\hat{q}_B/d=2/\sqrt{3}$).

Note in passing that in the pre-buckling case $P<1$ the expression for the fundamental frequency ω_1 of the straight beam can be obtained from Eq. (A10) by setting $q_B=0$, which yields the value $\omega_1=\omega_1^0\sqrt{1-P}$. One can conclude therefore that the sensitivity of the frequency to the axial force in the buckled configuration is two times higher than in the pre-buckled case.

The fundamental frequency of microbridges in the first buckled configuration f_0 can therefore be approximated by the expression

$$f_0 = 2\pi\sqrt{\frac{2EI}{3mL^4}\left(\frac{\sigma}{\sigma_E}-1\right)} \tag{A14}$$

where σ is the axial compressive stress and $\sigma_E = 4\pi^2 Er^2/L^2$ is the Euler's buckling stress.

REFERENCES

1. Blom, F., Bouwstra, S., Elwenspoek, M. & Fluitman, J. Dependence of the quality factor of micromachined silicon beam resonators on pressure and geometry. J. Vac. Sci. Technol. B 10 (1992).

2. Bianco, S. et al. Silicon resonant microcantilevers for absolute pressure measurement. Journal of Vacuum Science & Technology B 24, 1803-1809 (2006).

3. Jha, C. M. et al. High resolution microresonator-based digital temperature sensor. Applied Physics Letters 91 (2007).

4. LaHaye, M. D., Buu, O., Camarota, B. & Schwab, K. C. Approaching the Quantum Limit of a Nanomechanical Resonator. Science 304, 74-77 (2004).

5. Bleszynski-Jayich, A. C., Shanks, W. E. & Harris, J. G. E. Noise thermometry and electron thermometry of a sample-on-cantilever system below 1 Kelvin. Applied Physics Letters 92, 013123 (2008).

6. Cleland, A. N. & Roukes, M. L. A nanometre-scale mechanical electrometer. Nature 392, 160-162 (1998).

7. Rugar, D., Budakian, R., Mamin, H. J. & Chui, B. W. Single spin detection by magnetic resonance force microscopy. Nature 430, 329-332 (2004).

8. Ilic, B. et al. Mechanical resonant immunospecific biological detector. Applied Physics Letters 77, 450-452 (2000).

9. Ilic, B. et al. Attogram Detection Using Nanoelectromechanical Oscillators. Journal of Applied Physics **95**, 3694 (2004).

10. Ilic, B., Yang, Y. & Craighead, H. G. Virus detection using nanoelectromechanical devices. Applied Physics Letters 85, 2604 (2004).

11. Ilic, B. et al. Enumeration of DNA Molecules Bound to a Nanomechanical Oscillator. Nano Letters 5, 925-929 (2005).

12. Ekinci, K. L., Huang, X. M. H. & Roukes, M. L. Ultrasensitive nanoelectromechanical mass detection. Applied Physics Letters 84, 4469-4471 (2004).

13. Yang, Y., Callegari, C., Feng, X., Ekinci, K. & Roukes, M. Zeptogram-Scale Nanomechanical Mass Sensing. Nano Letters 6, 583-586 (2006).

14. Burg, T. P. & Manalis, S. R. Suspended microchannel resonators for biomolecular detection. Applied Physics Letters 83, 2698-2700 (2003).

15. Burg, T. P. et al. Weighing of biomolecules, single cells and single nanoparticles in fluid. 446, 1066-1069 (2007).

16. W. E. Newell, Science 161, 1320 (1968).

17. H. G. Craighead, Science 290, 1532 (2000).

18. A. Manz, N. Graber, and H. M. Widmer, Sens. Actuators B 1, 244 (1990).

19. D. Janasek, J. Franzke, and A. Manz, Nature 442, 374 (2006).

20. P. S. Waggoner, H. G. Craighead, Lab Chip 7, 1238, (2007).

21. J. L. Arlett, E. B. Myers, and M. L. Roukes, Nat. Nanotechnol. 6, 203 (2011).

22. R. A. Dweik and A. Amann, J. Breath Res. 2, 030301 (2008).

23. A. Deykin, J. Allergy Clin. Immunol. 118, 565 (2006).

24. D. Schmid, H. Lang, S. Marsch, C. Gerber, and P. Hunziker, Eur. J. Nanomed. 1, 44 (2008).

25. L. A. Pinnaduwage, V. Boiadjiev, J. E. Hawk, and T. Thundat, Appl. Phys. Lett. 83, 1471 (2003).

26. J. Bowen, L. J. Noe, B. P. Sullivan, K. Morris, V. Martin, and G. Donnelly, Appl. Spectrosc. 57, 906 (2003).

27. A. R. Krause, C. Van Neste, L. Senesac, T. Thundat, and E. Finot, J. Appl. Phys. 103, 094906 (2008).

28. Y. Engel, R. Elnathan, A. Pevzner, G. Davidi, E. Flaxer, and F. Patolsky, Angew. Chem. Int. Ed. 49, 6830 (2010).

29. F. M. Battiston, J.-P. Ramseyer, H. P. Lang, M. K. Baller, Ch. Gerber, J. K. Gimzewski, E. Meyer, and H.-J. Gu¨ntherodt, Sensor Actuators B 77, 122 (2001).

30. A. Bietsch, J. Zhang, M. Hegner, H. P. Lang, and C. Gerber, Nanotechnology 15, 873 (2004).

31. N. S. Lewis, Acc. Chem. Res. 37, 663 (2004).

32. A. M. Kummer, A. Hierlemann, and H. Baltes, Anal. Chem. 76, 2470 (2004).

33. Q. Wan, Q. H. Li, Y. J. Chen, T. H. Wang, X. L. He, J. P. Li, and C. L. Lin, Appl. Phys. Lett. 84, 3654 (2004).

34. D. A. Buttry and M. D. Ward, Chem. Rev. 92, 1355 (1992).

35. J. W. Grate, S. L. Rosepehrsson, D. L. Venezky, M. Klusty, and H. Wohltjen, Anal. Chem. 65, 1868 (1993).

36. K. Bodenhofer, A. Hierlemann, G. Noetzel, and W. G opel, Anal. Chem. 68, 2210 (1996).

37. M. Li, E. B. Myers, H. X. Tang, S. J. Aldridge, H. C. McCraig, J. J. Whiting, R. J. Simonson, N. S. Lewis, and M. L. Roukes, Nano Lett. 10, 3899 (2010).

38. A. Boisen, S. Dohn, S. S. Keller, S. Schmid, and M. Tenje, Rep. Prog. Phys. 74, 036101 (2011).

39. D. R. Southworth, L. M. Bellan, Y. Linzon, H. G. Craighead, and J. M. Parpia, Appl. Phys. Lett. 96, 163503 (2010). (Erratum in: Appl. Phys. Lett. 98, 139901 (2011)).

40. W. L. Hallauer, C. Ma, J. Micromech Microeng. 21, 065025 (2011).

41. K. S. Novoselov, a K. Geim, S. V Morozov, D. Jiang, Y. Zhang, S. V Dubonos, I. V Grigorieva, a a Firsov, Science, 306, 666–9 (2004).

42. Y. Zhang, Y.-W. Tan, H. L. Stormer, P. Kim, Nature, 438, 201–204 (2005).

43. G. Nanoelectronics, C. Berger, Z. Song, T. Li, X. Li, A. Y. Ogbazghi, R. Feng, Z. Dai, A. N. Marchenkov, E. H. Conrad, P. N. First, W. A. De Heer, 19912–19916 (2004).

44. K. I. Bolotin, K. J. Sikes, Z. Jiang, M. Klima, G. Fudenberg, J. Hone, P. Kim, H. L. Stormer, 1–5 (2008).

45. S. Das, M. Kim, J. Lee, W. Choi, Crit. Rev. Solid State Mater. Sci., 39, 231–252 (2014).

46. Y. Huang, X. Dong, Y. Shi, C. M. Li, L.-J. Li, P. Chen, Nanoscale, 2, 1485–8 (2010).

47. M. Kim, J. Hwang, L. A. Lepak, J. Lee, M. G. Spencer, S. Tiwari, Nanotechnology, 23, 335202 (2012).

48. K. S. Kim, Y. Zhao, H. Jang, S. Y. Lee, J. M. Kim, K. S. Kim, J.-H. Ahn, P. Kim, J.-Y. Choi, B. H. Hong, Nature, 457, 706–10 (2009).

49. R. A. Barton, J. Parpia, H. G. Craighead, J. Vac. Sci. Technol. B Microelectron. Nanom. Struct., 29, 050801 (2011).

50. Y. Liu, X. Dong, P. Chen, Chem. Soc. Rev. 41, 2283 (2012).

51. S. Wu, Q. He, C. Tan, Y. Wang, H. Zhang, Small, 9, 1160–72 (2013).

52. F. Schedin, a K. Geim, S. V Morozov, E. W. Hill, P. Blake, M. I. Katsnelson, K. S. Novoselov, Nat. Mater., 6, 652–5 (2007).

53. Y. Ohno, K. Maehashi, Y. Yamashiro, K. Matsumoto, Nano Lett., 9, 3318–3322 (2009).

54. Q. He, H. G. Sudibya, Z. Yin, S. Wu, H. Li, F. Boey, W. Huang, P. Chen, H. Zhang, ACS Nano, 4, 3201–3208 (2010).

55. T. Cohen-Karni, Q. Qing, Q. Li, Y. Fang, C. M. Lieber, Nano Lett., 10, 1098–102 (2010).

56. L. Feng, Y. Chen, J. Ren, X. Qu, Biomaterials, 32, 2930–7 (2011).

57. Y. Huang, X. Dong, Y. Liu, L.-J. Li, P. Chen, J. Mater. Chem., 21, 12358 (2011).

58. H. D. Jang, S. K. Kim, H. Chang, K.-M. Roh, J.-W. Choi, J. Huang, Biosens. Bioelectron., 38, 184–8 (2012).

59. M. Du, T. Yang, K. Jiao, J. Mater. Chem., 20, 9253 (2010).

60. B. Su, J. Tang, J. Huang, H. Yang, B. Qiu, G. Chen, D. Tang, Electroanalysis, 22, 2720–2728 (2010).

61. L. Feng, L. Wu, J. Wang, J. Ren, D. Miyoshi, N. Sugimoto, X. Qu, Adv. Mater., 24, 125–31 (2012).

62. D. Khatayevich, T. Page, C. Gresswell, Y. Hayamizu, W. Grady, M. Sarikaya, Small, 10, 1505–13, 1504 (2014).

63. H. J. Yoon, T. H. Kim, Z. Zhang, E. Azizi, T. M. Pham, C. Paoletti, J. Lin, N. Ramnath, M. S. Wicha, D. F. Hayes, D. M. Simeone, S. Nagrath, Nat. Nanotechnol., 8, 735–41 (2013).

64. T. Alava, J. a Mann, C. Théodore, J. J. Benitez, W. R. Dichtel, J. M. Parpia, H. G. Craighead, Anal. Chem., 85, 2754–9 (2013).

65. J. Hwang, M. Kim, D. Campbell, H. a Alsalman, J. Y. Kwak, S. Shivaraman, A. R. Woll, A. K. Singh, R. G. Hennig, S. Gorantla, M. H. Rümmeli, M. G. Spencer, ACS Nano, 7, 385–95 (2013).

66. J. Hwang, M. Kim, H. Cha, M. G. Spencer, J. Lee, J. Nanosci. Nanotechnol., 13, 1–5 (2013).

67. Jemal A. Cancer Statistics CA: A Cancer Journal for Clinicians, 57, 43-66 (2007).

68. Winawer S, Faivre J, Selby J, et al. Workgroup II: the screening process. UICC International Workshop on Facilitating Screening for Colorectal Cancer, Oslo, Norway (29 and 30 June 2002). Ann Oncol, 16, 31-3 (2005).

69. Valastyan S, Weinberg RA. Tumor metastasis: molecular insights and evolving paradigms. Cell, 147, 275-92 (2011).

70. Hanahan D, Weinberg RA. Hallmarks of cancer: the next generation. Cell, 144, 646-74 (2011).

71. D. M. Karabacak, S. H. Brongersma, and M. Crego-Calama, Lap Chip 10, 1976, (2010).

72. H. Kahn, R. Ballarini, and A. H. Heuer, J. Mater. Res. 17, 1855 (2002).

73. D. W. Carr and H. G. Craighead, J. Vac. Sci. Technol. B 15, 2760 (1997).

74. D. T. Turner, Polymer 23, 197 (1982).

75. R. B. Anderson, J. Bayer, and L. J. E. Hofer, Ind. Eng. Chem. Ind. Eng. Chem. Process Des. Dev 4, 167 (1965).

76. R. Chiba and N. Funakoshi, Thin Solid Films 157, 307 (1988).

77. J. J. Blech, J. Lubr. Technol. 105, 615 (1983).

78. S. S. Verbridge, R. Ilic, H. G. Craighead, and J. M. Parpia, Appl. Phys. Lett. 93, 013101 (2008).

79. D. R. Southworth, H. G. Craighead, and J. M. Parpia, Appl. Phys. Lett. 94, 213506 (2009).

80. R. A. Bidkar, R. C. Tung, A. A. Alexeenko, H. Sumali, and A. Raman, Appl. Phys. Lett. 94, 163117 (2009).

81. R. C. Tung, J. W. Lee, H. Sumali, and A. Raman, J. Micromech. Microeng. 21, 025003 (2011).

82. M. Bao, H. Yang, Sens. Actuators A 136, 3 (2007).

83. A. H. Nayfeh, W. Kreider, and T. J. Anderson, AIAA J. 33, 1121 (1995).

84. L. Nicu and C. Bergaud, J. Appl. Phys. 86, 5835 (1999).

85. S. A. Emam and A. H. Nayfeh, Nonlinear Dyn. 35, 1 (2004).

86. R. C. Tung RC, J. W. Lee, H. Sumali, and A. Raman, J. Micromech. Microeng. 21, 025003 (2011).

87. R. A. Bidkar, R. C. Tung, A. A. Alexeenko, H. Sumali, and A. Raman, Appl. Phys. Lett. 94, 163117 (2009).

88. H. Sumali, J. Micromech. Microeng. 17, 2231 (2007).

89. G. G. Fattinger and P. T. Tikka, Appl. Phys. Lett. 79, 290 (2001).

90. K. Kokkonen and M. Kaivola, Appl. Phys. Lett. 92, 063502 (2008).

91. C. Rembe and R. S. Muller, J. Microelectromech S. 11, 479 (2002).

92. Y. Linzon, S. Krylov, B. Ilic, D. R. Southworth, R. A. Barton, B. R. Cipriany, J. D. Cross, J. M. Parpia, and H. G. Craighead, Opt. Lett. 15, 2654 (2010).

93. J. D. Gaskill, Linear Systems, Fourier Transforms, and Optics (Wiley, New York, 1978).

94. M. Bass, Handbook of Optics, 2nd ed. (McGraw-Hill, San Francisco, 1995), Vol. I, pp. 42.10-42.14.

95. I. Voiculescu, M. E. Zaghloul, R. A. McGill, E. J. Houser, and G. K. Fedder, IEEE Sens. J. 5, 641 (2005).

96. Walters S, Maringe C, Butler J, Brierley JD, Rachet B, Coleman MP. Comparability of stage data in cancer registries in six countries: lessons from the International Cancer Benchmarking Partnership. International journal of cancer Journal international du cancer, 132, 676-85 (2013).

97. Ellis L.M. Preclinical data targeting vascular endothelial growth factor in colorectal cancer. Clinical colorectal cancer, 4 Suppl 2:S55-61 (2004).

98. Dimasi J.A, Reichert J.M, Feldman L, Malins A. Clinical approval success rates for investigational cancer drugs. Clinical pharmacology and therapeutics, 94, 329-35 (2013).

99. Rubio-Viqueira B, Hidalgo M. Direct in vivo xenograft tumor model for predicting chemotherapeutic drug response in cancer patients. Clinical pharmacology and therapeutics, 85, 217-21 (2009).

100. Sausville EA, Burger AM. Contributions of human tumor xenografts to anticancer drug development. Cancer research, 66, 3351-4 (2006).

101. Siolas D, Hannon GJ. Patient-Derived Tumor Xenografts: Transforming Clinical Samples into Mouse Models. Cancer research (2013).

102. Sikandar SS, Pate KT, Anderson S, et al. NOTCH signaling is required for formation and self-renewal of tumor-initiating cells and for repression of secretory cell differentiation in colon cancer. Cancer research 2010;70:1469-78.

103. Chen HJ, Edwards R, Tucci S, et al. Chemokine 25-induced signaling suppresses colon cancer invasion and metastasis. The Journal of clinical investigation 2012;122:3184-96.

104. Ebert MP, Tanzer M, Balluff B, et al. TFAP2E-DKK4 and chemoresistance in colorectal cancer. The New England journal of medicine 2012;366:44-53.

105. Meng RD, Shelton CC, Li YM, et al. gamma-Secretase inhibitors abrogate oxaliplatin-induced activation of the Notch-1 signaling pathway in colon cancer cells resulting in enhanced chemosensitivity. Cancer research 2009;69:573-82.

106. Denk W1, Strickler JH, Webb WW. Science. 1990 Apr 6;248(4951):73-6.

107. Martin Oheim, Darren J. Michael, Matthias Geisbauer, Dorte Madsen, Robert H. Chow, Advanced Drug Delivery Reviews 58 (2006) 788–808

108. Farrar MJ, Bernstein IM, Schlafer DH, Cleland TA, Fetcho JR, Schaffer CB. Chronic in vivo imaging in the mouse spinal cord using an implanted chamber. Nature methods 2012;9:297-302.

109. Kabelitz D, Wesch D. Features and functions of gamma delta T lymphocytes: focus on chemokines and their receptors. Crit Rev Immunol 2003;23:339-70.

110. Youn BS, Kim YJ, Mantel C, Yu KY, Broxmeyer HE. Blocking of c-FLIP(L)--independent cycloheximide-induced apoptosis or Fas-mediated apoptosis by the CC chemokine receptor 9/TECK interaction. Blood 2001;98:925-33.

111. Wurbel MA, McIntire MG, Dwyer P, Fiebiger E. CCL25/CCR9 interactions regulate large intestinal inflammation in a murine model of acute colitis. PLoS ONE 2011;6:e16442.

112. LaPointe LC, Dunne R, Brown GS, et al. Map of differential transcript expression in the normal human large intestine. Physiol Genomics 2008;33:50-64.

113. Li X, Madison BB, Zacharias W, Kolterud A, States D, Gumucio DL. Deconvoluting the intestine: molecular evidence for a major role of the mesenchyme in the modulation of signaling cross talk. Physiol Genomics 2007;29:290-301.

114. Cancer Genome Atlas N. Comprehensive molecular characterization of human colon and rectal cancer. Nature 2012;487:330-7.

115. Lautt WW. Mechanism and role of intrinsic regulation of hepatic arterial blood flow: hepatic arterial buffer response. The American journal of physiology 1985;249:G549-56.

116. Thiel H. Liver hemodynamics and portacaval shunt. Surgery, gynecology & obstetrics 1980;150:587-92.

117. Dancis J. Transport of substances across perfused organs. Acta endocrinologica Supplementum 1972;158:347-75.

118. Vanharanta S, Massague J. Hypoxia signaling--license to metastasize. Cancer discovery 2013;3:1103-4.

119. Vanharanta S, Massague J. Origins of metastatic traits. Cancer cell 2013;24:410-21.

120. Chaturvedi P, Gilkes DM, Wong CC, et al. Hypoxia-inducible factor-dependent breast cancer-mesenchymal stem cell bidirectional signaling promotes metastasis. The Journal of clinical investigation 2013;123:189-205.

121. Eisinger-Mathason TS, Zhang M, Qiu Q, et al. Hypoxia-dependent modification of collagen networks promotes sarcoma metastasis. Cancer discovery 2013;3:1190-205.

122. Erler JT, Bennewith KL, Nicolau M, et al. Lysyl oxidase is essential for hypoxia-induced metastasis. Nature 2006;440:1222-6.

123. Gilkes DM, Chaturvedi P, Bajpai S, et al. Collagen prolyl hydroxylases are essential for breast cancer metastasis. Cancer research 2013;73:3285-96.